A dusty filament and turbulent CO spirals in HD 135344B - SAO 206462

Simon Casassus [1]★ Valentin Christiaens [2] Miguel Cárcamo [3,4,5] Sebastián Pérez [5,6] Philipp Weber,[1,6] Barbara Ercolano,[7] Nienke van der Marel [8] Christophe Pinte [2,9] Ruobing Dong,[8] Clément Baruteau [10] Lucas Cieza,[11] Ewine F. van Dishoeck [12,13] Andrés Jordan [14,15] Daniel J. Price [2] Olivier Absil [16] Carla Arce-Tord,[1] Virginie Faramaz,[17] Christian Flores [18] and Maddalena Reggiani[19]

Affiliations are listed at the end of the paper

ABSTRACT

Planet–disc interactions build up local pressure maxima that may halt the radial drift of protoplanetary dust, and pile it up in rings and crescents. ALMA observations of the HD 135344B disc revealed two rings in the thermal continuum stemming from $\sim$mm-sized dust. At higher frequencies the inner ring is brighter relative to the outer ring, which is also shaped as a crescent rather than a full ring. In near-IR scattered light images, the disc is modulated by a two-armed grand-design spiral originating inside the ALMA inner ring. Such structures may be induced by a massive companion evacuating the central cavity, and by a giant planet in the gap separating both rings, that channels the accretion of small dust and gas through its filamentary wakes while stopping the larger dust from crossing the gap. Here we present ALMA observations in the $J = (2 - 1)$ CO isotopologue lines and in the adjacent continuum, with up to 12 km baselines. Angular resolutions of $\sim0\!\!.\!\!''03$ reveal the tentative detection of a filament connecting both rings, and which coincides with a local discontinuity in the pitch angle of the IR spiral, proposed previously as the location of the protoplanet driving this spiral. Line diagnostics suggests that turbulence, or superposed velocity components, is particularly strong in the spirals. The ^{12}CO(2-1) 3D rotation curve points at stellocentric accretion at radii within the inner dust ring, with a radial velocity of up to $\sim$5 per cent $\pm$ 0.5 per cent Keplerian, which corresponds to an excessively large accretion rate of $\sim 2 \times 10^{-6}\,M_\odot\,\mathrm{yr}^{-1}$ if all of the CO layer follows the ^{12}CO(2-1) kinematics. This suggests that only the surface layers of the disc are undergoing accretion, and that the line broadening is due to superposed laminar flows.

Key words: protoplanetary discs – accretion, accretion discs – planet–disc interactions.

1 INTRODUCTION

The radial drift of protoplanetary dust halts at local pressure maxima (Weidenschilling 1977), where the azimuthal gaseous flow exerts no net drag. The pile-up of dust with dimensionless stopping time (Stokes number) $S_t \lesssim 1$ in radial pressure bumps, whichever their origin, explains the Atacama Large Millimeter/submillimeter Array (ALMA) observations of dusty ringed systems, such as reported in HLTau (ALMA Partnership 2015; Carrasco-González et al. 2019), in HD 169142 (e.g. Pérez et al. 2019; Sierra et al. 2019), or in the DSHARP survey (Andrews et al. 2018; Dullemond et al. 2018).

The same radial pressure discontinuities leading to radial trapping can also trigger the Rossby-wave instability, and develop a large-scale anti-cyclonic vortex (Lovelace et al. 1999; Li et al. 2001) resulting in strong radial and azimuthal concentration for $S_t \lesssim 1$ dust grains (Birnstiel, Dullemond & Pinilla 2013; Lyra & Lin 2013; Zhu & Stone 2014; Mittal & Chiang 2015; Baruteau & Zhu 2016). The radial pressure discontinuity itself could result from the formation of a planetary gap (Zhu & Stone 2014; Koller, Li & Lin 2003; de Val-Borro et al. 2007; Zhu & Baruteau 2016), among other possibilities (e.g. Varnière & Tagger 2006; Regály et al. 2012).

Azimuthal dust traps have been identified observationally with ALMA in the form of large-scale crescents of continuum submillimeter emission, with extreme azimuthal contrast ratios of $\sim$30 in HD 142527 (Casassus et al. 2013, 2015; Muto et al. 2015; Boehler et al. 2017) and $\sim$ 100 in IRS 48 (van der Marel et al. 2013, 2015b; Ohashi et al. 2020). Such extreme lopsidedness, in combination with an otherwise full gas disc as revealed by CO observations, has been interpreted as likely due to dust trapping in a vortex (Birnstiel et al. 2013; Lyra & Lin 2013; Baruteau & Zhu 2016; Sierra, Lizano & Barge 2017). Finer ALMA angular resolutions have revealed that crescents with varying contrast ratios are fairly frequent in the outer rings of ringed systems, such as in LkHα330 (Isella et al. 2013), SR 21, HD 135344B (Pérez et al. 2014; van der Marel et al. 2015a, 2016b; Cazzoletti et al. 2018), DoAr 44 (van der Marel et al. 2016a), and HD 34282 (van der Plas et al. 2017). The occurrence of such asymmetries is associated with Stokes numbers $S_t \lesssim 1$, in agreement with the dust trapping scenario (e.g. van der Marel et al. 2021). In the brighter clump of MWC 758 at VLA frequencies, the multi-frequency continuum observations can be reproduced with the Lyra-Lin trapping prescriptions, which yields estimates of the local physical conditions and constraints on the dust population (Marino et al. 2015; Casassus et al. 2019).

Similar processes as in protoplanetary discs are thought to have occurred in the protosolar disc. The statistics of meteoritic inclusions

★ E-mail: simon@das.uchile.cl

provide important information on the physical processes that shaped the Solar System. The same gapped system predicted for an accreting proto-Jupiter also accounts for the filtering of the larger dust grains out of the inner disc, and explains the size distributions of meteoritic inclusions (Haugbølle et al. 2019). Multi-fluid simulations including dust and gas show that the smaller dust population sieves across the proto-jovian gap through the planetary wakes, i.e. as in the bottleneck of an hourglass which prevents the larger dust from crossing the gap, with the maximum grain size permitted to cross depending on disc characteristics (e.g. Weber et al. 2018). It is interesting to search for similar features in exo-protoplanetary systems as required to explain the meteoritic inclusions: smaller dust grains in the inner regions of protoplanetary discs hosting deep gaps. Such inner dust discs are frequently detected, and appear to be depleted in mm-dust mass (e.g. Francis & van der Marel 2020).

The disc around HD 135344B, also called SAO 206462 (with a spectral type F8V, and at a distance of 135.7 ± 1.4 pc, Gaia Collaboration 2018), is particularly interesting because of several planet-formation signposts, as its sub-millimeter continuum emission is essentially composed of two rings, at 0″.4 (52 au) and 0″.6 (80 au) separated by a deep and broad gap, and crossed by a grand-design two-armed spiral prominent in scattered-light images (Stolker et al. 2016). The two arms of this spiral pattern have been proposed to be driven by two planets orbiting at ∼0″.4 and ∼0″.9 (so ∼54 and ∼121.5 au, Muto et al. 2012), or from a massive planet inside the cavity at ∼0″.23 along with the outer disc vortex (van der Marel et al. 2016a,b), or the whole pattern could result from gravitational instability (GI, Dong et al. 2015; Dong, Najita & Brittain 2018b). Multi-epoch monitoring of the scattered-light spirals has allowed the measurement of the pattern motion, which points at a companion at 86^{+18}_{-13} au if the arms are co-moving, or else to two companions at 49^{+6}_{-5} au and 120 ± 30 au (Xie et al. 2021). The multi-wavelength imaging reported by Cazzoletti et al. (2018) supports an interpretation in terms of the filtering of the larger dust grains out of the inner regions, since the inner ring is increasingly brighter at higher frequencies compared to the outer ring. This brightness effect could also point to a difference in dust evolution within the two rings, i.e. to different fragmentation rates.

Here we report on new ALMA observations of HD 135344B (Section 2) that reveal the tentative detection of the dusty protoplanetary wakes predicted by theory. A narrow trickle of dust continuum emission seems to connect the lopsided outer ring with the inner ring (Section 3), close to the planet at ∼0″.4 proposed by Muto et al. (2012). A simple analysis of the line emission reveals that the two-armed spiral corresponds to enhanced velocity dispersions (Section 3). We interpret the available data in terms of disc-surface accretion towards the star (Section 4).

2 OBSERVATIONS

HD 135344B was observed with ALMA during Cycle 6, as part of program 2018.1.01066.S. The data presented in this article correspond to a partial delivery of the whole program, which is scheduled for execution in Cycle 7 with a nominal 13 h of telescope time. In this partial data set, HD 135344B was observed from 13-Jul-2019/02:43:39 to 13-Jul-2019/03:55:34 (UTC), for a total of 43 min on-source. The phase centre of the array pointed at J2000 15h15m48.4142s −37d09m16.4776s, which is offset by 5.8 mas from the ICRS position of the star at the epoch of observations, J2000 15h15m48.4147s −37d09m16.4785s. The array counted 43 active antennas, with baselines ranging from 111.2 m to 12.6 km. The column of precipitable water vapour (PWV) ranged from

0.9 mm at the beginning of the integration, to 0.7 mm at the end. The correlator was setup to provide four spectral windows (spws): spw 0, sampling the continuum around 218 GHz with 128 channels over a total bandwidth of 2 GHz; spw 1, for ^{12}CO(2-1) at a rest frequency of 230.538 GHz, sampled with 158.74 m s^{-1} channels; spw 2, sampling the continuum around 232 GHz with 960 channels over a total bandwidth of 1.875 GHz; spw 3, for C^{18}O(2-1) at a rest frequency of 219.560 GHz, sampled with 166.68 m s^{-1} channels; spw 4, for ^{13}CO(2-1) at a rest frequency of 220.399 GHz, sampled with 166.04 m s^{-1} channels. The data were calibrated by staff from the North America ALMA Regional Centre.

Spectral windows spw 0 and spw 2 were devoid of conspicuous line emission and were combined to image the continuum. A single self-calibration loop, setting up CASA task gaincal to average whole scans (option 'solint' set to 'inf'), provided an improvement in tclean images using Briggs weights with robustness parameter $r = 0.0$, with a dynamic range (i.e. signal-to-noise ratio) increasing from ∼14.8 to ∼17.3. The quantitative improvement was small but the self-calibration loop got rid of noisy patches, so we adopted the self-calibrated data set. We then applied the UVMEM package (Casassus et al. 2006; Cárcamo et al. 2018) on the self-calibrated continuum data to produce a non-parametric model image. In brief, UVMEM produces a model-image I_j^m and model visibilities V_k^m that fit the visibility data V_k° in a least-square sense, with the possible inclusion of a regularizing term, by minimizing a figure of merit L:

$$L = \sum_{k=1}^{N_{vis}} \omega_k |V_k^\circ - V_k^m|^2 + \lambda S, \qquad (1)$$

where ω_k correspond to the visibility weights and the sum runs over all visibility data (i.e. without gridding). The term λS in equation (1) is a regularization term, whose functional definition depends on the application. In this case image positivity provided sufficient regularization, so we restricted the optimization to the least-squares term only (see for example Casassus et al. 2018, 2019, for example regularization terms and detailed applications of UVMEM to ALMA data in protoplanetary discs).

As summarized in Fig. 1, the continuum data are consistent with the general structure of the disc previously reported by Cazzoletti et al. (2018). The disc is composed of two main features: an outer ring shaped into a large crescent, as expected for a vortex (e.g. Baruteau & Zhu 2016), and an inner ring that at this frequency appears fainter relative to the outer ring. Here we also notice a faint plateau or pedestal abut on to the inner ring, and enclosing an otherwise very deep cavity. The central source, probably related to the star, shows signal at 5σ, with intriguing structure the details of which should be ascertained in second epoch imaging.

When integrated over the whole field plotted in Fig. 1, the continuum flux density at 225 GHz from HD 135344B is 117.4 ± 0.1 mJy in the Briggs 2.0 image, with a noise of ∼18 μJy beam^{-1}, and 105.1 ± 0.3 mJy in the Briggs 0.0 image, with a noise of ∼24 μJy beam^{-1}. The noise in the uvmem model image is positive definite, but we quote the integrated flux density for completeness, of 114.6 ± 1 mJy with a noise of ∼1 μJy pix^{-1} (corresponding to the peak signal of the spurious features away from the source). The thermal uncertainty is very small, but both values are affected by a systematic uncertainty of ∼10 per cent root-mean-square (rms). The nominal maximum recoverable angular scale (MRS) for this array configuration is ∼0″.62 (as given in the ALMA proposer's guide for Cycle 6), and since the continuum signal extends over ∼1″.2, there may be a measure of flux loss, i.e. missing low spatial frequencies in the reconstructed image due to missing short-spacings in the uv
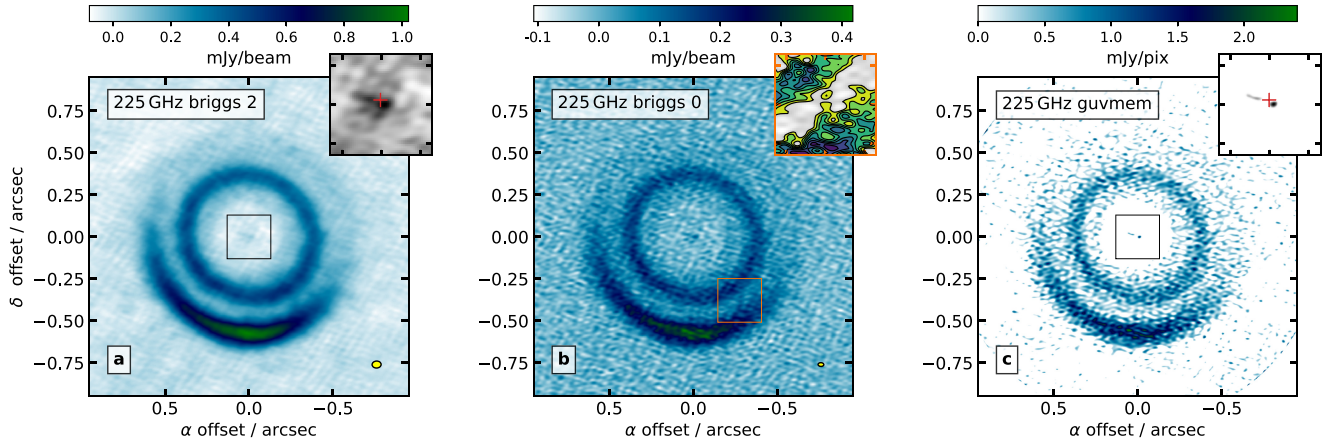
Figure 1. Continuum imaging in HD 135344B. (a) CASA-`tclean` image with Briggs robustness parameter $r = 2.0$ (so close to natural weights), resulting in a clean beam of $0\farcs054 \times 0\farcs041 / -87$ deg, where we give the beam major axis (bmaj), minor axis (bmin) and direction (bpa) in the format bmaj×bmin/bpa. b: CASA-`tclean` image with Briggs robust parameter 0.0, with a clean beam $0\farcs034 \times 0\farcs022 / 88$ deg c: UVMEM model image, with an effective angular resolution of $\sim 1/3$ of the natural-weights beam, or $\sim 0\farcs018 \times 0\farcs014 / -87$ deg. The insets in (a) and (c) zoom inside the central emission, where the centroid of the inner ring is marked by a red symbol (see Section 3.1 for details). The inset in (b) zooms on the filament with contour levels starting at 4σ and incremented in units of σ (the centre of this inset is at $[-0\farcs276, -0\farcs378]$). The tick-marks in the insets are separated by $0\farcs1$.

−coverage. The slightly lower flux in Briggs 0.0 compared to Briggs 2.0 may perhaps reflect this flux loss effect. But the total missing flux must be fairly small, as there are no obvious image synthesis artefacts that modulate the signal.

The line datacubes were extracted following a standard procedure, and after propagating the self-calibration gain tables to the full data set. Continuum subtraction was performed using CASA task `uvcontsub`, and using a linear model that avoids the vicinity of the lines. The data were then resampled into the local standard of rest, and using spectral channels with a width of 0.2 km s^{-1}, common to all lines. In an initial attempt at imaging synthesis, the resulting datacubes were first imaged with CASA task `tclean`, in its multi-scale version, with automatic masking (as implemented in the 'auto-multithresh' option to `tclean`), and using Briggs $r = 2.0$. In the case of the ^{12}CO(2-1) line, the peak signal is ~ 18 mJy beam^{-1}, while the noise (including image synthesis residuals) is 2.2 mJy beam^{-1} (for a beam $0\farcs054 \times 0\farcs040/89.4$ deg^1).

The resulting channel maps are shown in Appendix A. Imaging the ^{12}CO(2-1) datacubes is particularly challenging because this preliminary data release did not include data acquired in a complementary compact configuration. This results in strong aliasing in the restored images, as can be assessed by inspection of the channel maps in Fig. A1.

In an effort to overcome the systematics due to image synthesis, we also explored a different strategy using our UVMEM package. We proceeded as for the continuum emission, but this time including an entropic term for regularization as the data are quite noisy. We minimized L in equation (1) with

$$S = \sum_{j=1}^{N_{\text{pix}}} \frac{I_j^m}{M} \ln\left(\frac{I_j^m}{M}\right), \qquad (2)$$

where the sum runs over all pixels in the image (or within a user-defined region enclosing the signal), and M is the default pixel

intensity value, and is set to 10^{-3} times the theoretical noise of the dirty map (as inferred from the visibility weights). Here we use a control factor $\lambda = 1 \times 10^{-3}$. An important difference between UVMEM and `tclean` is that `tclean` uses masks to select regions in the sky which correspond to signal. These masks are adjusted iteratively in `tclean`. Initial trials with blind reconstructions using UVMEM, i.e. without applying masks, yielded similar results as for the `tclean` reconstructions. The restored datacubes, obtained using the UVMEM model datacube and Briggs $r = 2$, yielded a similar dynamic range as with `tclean`, but are less clumpy and more sensitive to extended signal. However, we also attempted the implementation in UVMEM of masks in channel maps, similar to those used by `tclean`. We used a rough approximation to Keplerian masks, using the tools^2 developed. The use of masks, as in `tclean`, resulted in an important improvement in dynamic range, as can be judged by comparing the `tclean` channel maps with the UVMEM channel maps shown in Fig. A2. The data from the rarer isotopologues are much noisier and compact and their dynamic range is limited by thermal noise rather than synthesis imaging artefacts, and indeed UVMEM did not provide improvements in their cases.

In order to trace the whole disc and extend the field of the isotopologue analysis presented below, we smoothed the data with a circular Gaussian taper, applied in the *uv*-plane, with a width of 50 mas. The resulting tapered beam is $\sim 0\farcs1 \times 0\farcs08/0$ deg (see caption to Fig. 2). These tapered versions of the data were again imaged using UVMEM with Keplerian masks, but without entropic regularization (so with $\lambda = 0$).

The moments maps shown in Fig. 2 were extracted using single-Gaussian fits to each datacube using package GMOMENTS.^{3} This package fits the line profile in each line of sight with either one or two Gaussians, and uses these model Gaussian line profiles to calculate the velocity moments. For a single Gaussian with $I_v = I_\circ \exp(-\frac{v - v^\circ}{\sigma_v})$ the line intensity is given by moment 0, or $I_{\text{Gauss}} = \sqrt{2\pi} I_\circ \sigma_v$, while the velocity centroid matches the Gaussian

---

^{1}expressed in the form (BMAJ×BMIN / BPA), where BMAJ and BMIN are the full-width major and minor axis, and BPA is the beam PA in degrees East of North.

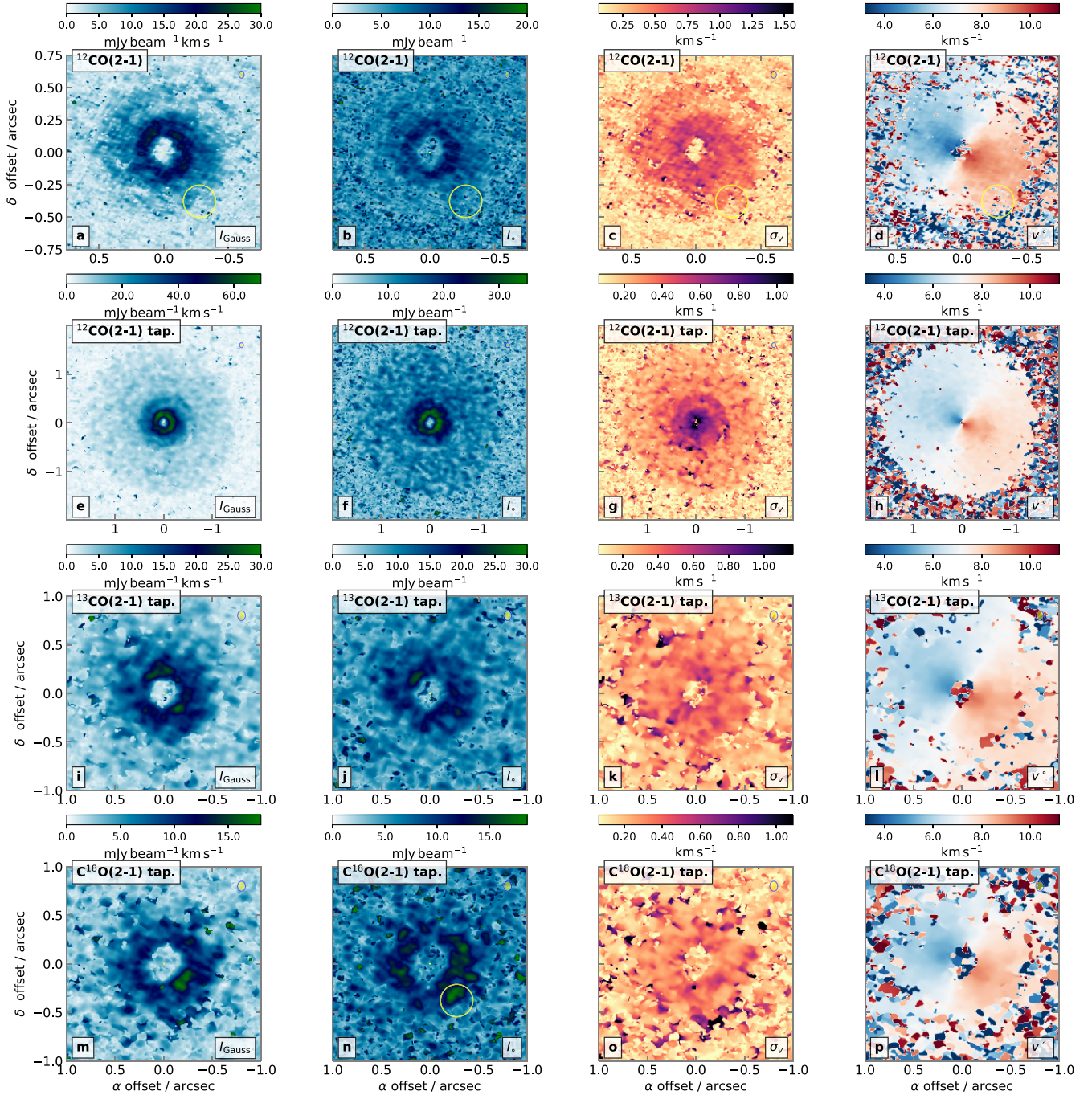^{2}https://github.com/richteague/keplerian_mask
^{3}https://github.com/simoncasassus/GMoments

Figure 2. Moment maps in ^{12}CO(2-1), ^{13}CO(2-1) and C^{18}O(2-1) extracted from the uvmem datacubes using single-Gaussian fits in velocity. The yellow circle marks the same region of interest as in Fig. 1b. The first row shows, for ^{12}CO(2-1), (a) the Gaussian velocity-integrated intensity $I_{\rm Gauss}$, (b) the Gaussian amplitude $I_\circ$, (c) the Gaussian dispersion σ_v, and (d) the Gaussian velocity centroid $v_\circ$. The beam ($0\farcs054 \times 0\farcs040$ / 0 deg) is indicated by a yellow ellipse. The second to fourth rows extend the same images to tapered versions of ^{12}CO(2-1) ($0\farcs100 \times 0\farcs081$ / 0 deg beam), ^{13}CO(2-1) ($0\farcs100 \times 0\farcs081$ / 0 deg beam), and C^{18}O(2-1) ($0\farcs102 \times 0\farcs082$ / 0 deg beam). Note the larger field of view for e)-h).

centroid. We note that the two-armed grand-design spiral that stands out in the ^{12}CO velocity-integrated intensity and velocity dispersion, but that is absent in the line peak intensity. These ^{12}CO data do not appear to be affected by the underlying continuum in the large crescent: continuum subtraction does not lead to any local decrement in the tapered images, and ^{12}CO(2-1) emission is seen to extend out to radii of $\sim 1\farcs1$. We note, however, an

arc-like decrement seen in the Gaussian amplitude in Fig. 2f, that is abut on the continuum so coincident with the gap in between the two rings. Another particularly interesting feature of the channel maps is the local ^{18}CO(2-1) peak coincident with the location of the candidate filament (Fig. 2n). This local peak is particularly strong in the ^{18}CO(2-1) channel maps at $v_{\rm lsr} \sim 8.5\,{\rm km\,s^{-1}}$.
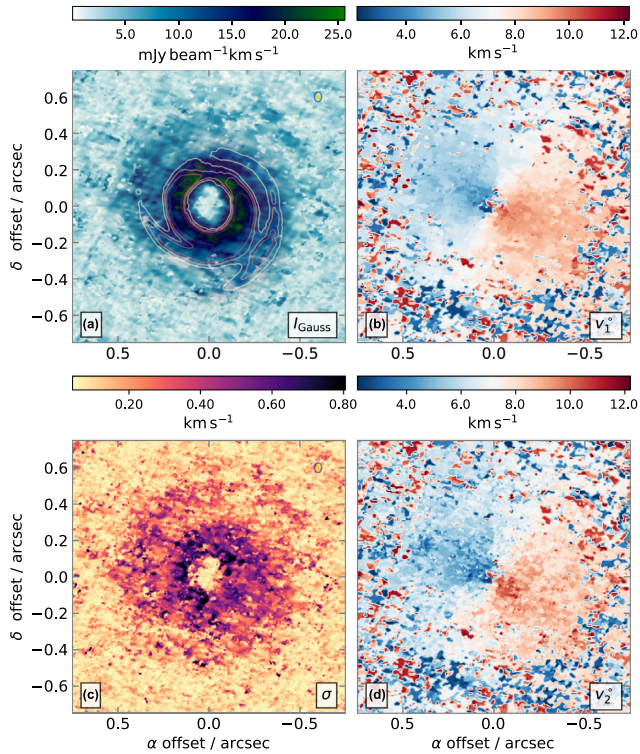
Figure 3. Moment maps in $^{12}CO(2-1)$ extracted from the UVMEM-restored datacube using double-Gaussian fits in velocity, and comparison with the H−band polarized intensity. (a) The 2-Gaussian velocity-integrated intensity in colour scale, compared with the H−band Q_ϕ image from Fig. 4, traced with the same contours (see Section 3.2). b) The velocity centroid of the brighter Gaussian. (c) The Gaussian dispersion. (d) The velocity centroid of the fainter Gaussian.

The top and bottom $^{12}CO(2-1)$ layers are sufficiently separated in this disc to trace each layer with a double-Gaussian fit, as summarized in Fig. 3 for the untapered UVMEM-restored datacube. We assume that the brighter of the two Gaussians traces the top side, that faces the observer. The velocity-integrated intensity is very similar to the single-Gaussian case, as is the Gaussian velocity dispersion. Interestingly, the disc PA inferred from the velocity centroid of the brighter Gaussian, v_1°, shifts slightly to the North-West with increasing distance from the star, as expected for the surface of a cone in which the side nearest to the observer is to the South-East. However, the velocity centroid v_2° corresponding to the fainter Gaussian, shifts progressively to the South-East, indicating that it is indeed tracing the bottom layer. This suggests that the extended disc and the spiral modulation seen in dispersion is intrinsic to the top (or bottom) layer, and is not the result of broadening due to a second velocity component stemming from the bottom layer.

3 ANALYSIS

3.1 Continuum filament and disk orientation

The 225 GHz continuum image reported in Fig. 1 reveals interesting fine structure in the gap that divides the inner and outer rings. A very fine filament appears to join the two rings, at a radial separation of ∼0.′′468 (63.5 au) and PA ∼ 216.1 deg, as highlighted in Fig. 1b. It is best seen in the tclean image with Briggs $r = 0$, where the median intensity in a region isolating the filament is 104 μJy beam^{-1}, and the
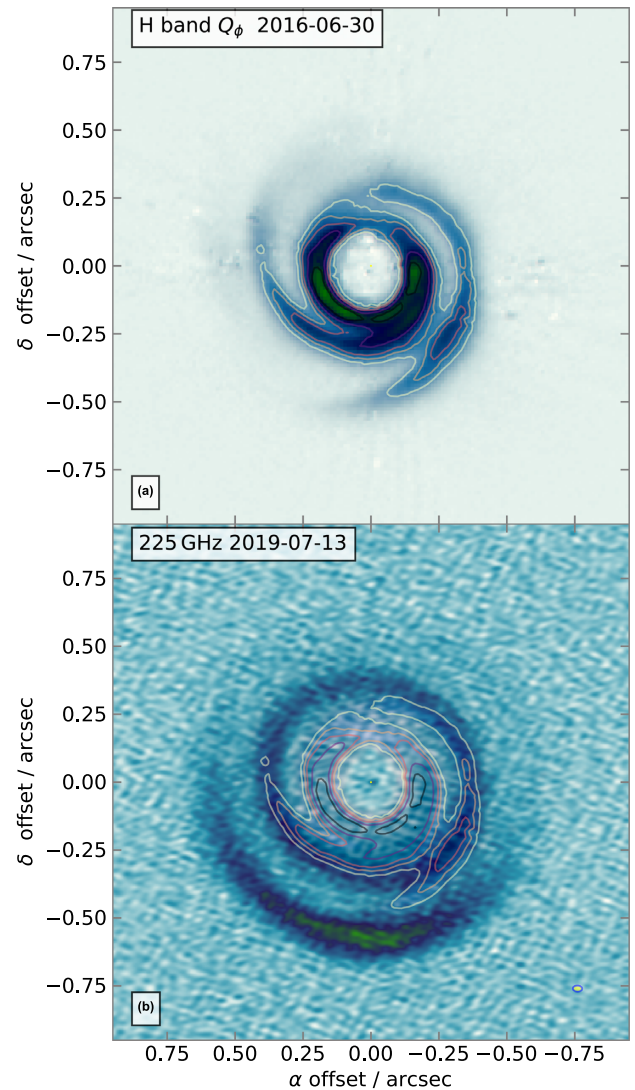

Figure 4. (a) IRDAP reduction of the H-band Q_ϕ image data from Stolker et al. (2017), with contours taken at peak-intensity fractions of 0.2, 0.3, 0.4, 0.6, 0.8. (b) Overlay of the same contours as in (a) on the Briggs $r = 0$ image from Fig. 1b.

noise is 24 μJy beam^{-1}. While this would appear as a 4σ detection, there are other fine features in the same gap at a similar intensity level, although these other features are smaller and appear to sprout away from either the inner or outer ring (and may also be real). These other features suggest that the detection of this filament should be considered as a tentative result, whose confirmation requires deeper observations. We note, however, in Section 3.2 that the filament is similar in shape and pitch angle as a trailing spiral arm, and that it is almost coincident with a twist observed in the near-IR spirals reported in Muto et al. (2012) and Stolker et al. (2016), which supports the idea that the filament, if real, may be tracing gap-crossing planetary wakes.

Fig. 4 compares the ALMA continuum image of HD 135344 B with the polarized intensity image of the disc that was acquired with VLT/SPHERE on 2016-06-30. This Q_ϕ image (see definitions in Avenhaus et al. 2014; Garufi et al. 2014) of HD 135344 B is the one obtained in the best seeing conditions (average 0.5-μm seeing of 0.′′37; Stolker et al. 2017), and is therefore favoured throughout the rest of this work for comparison to our ALMA data. We re-
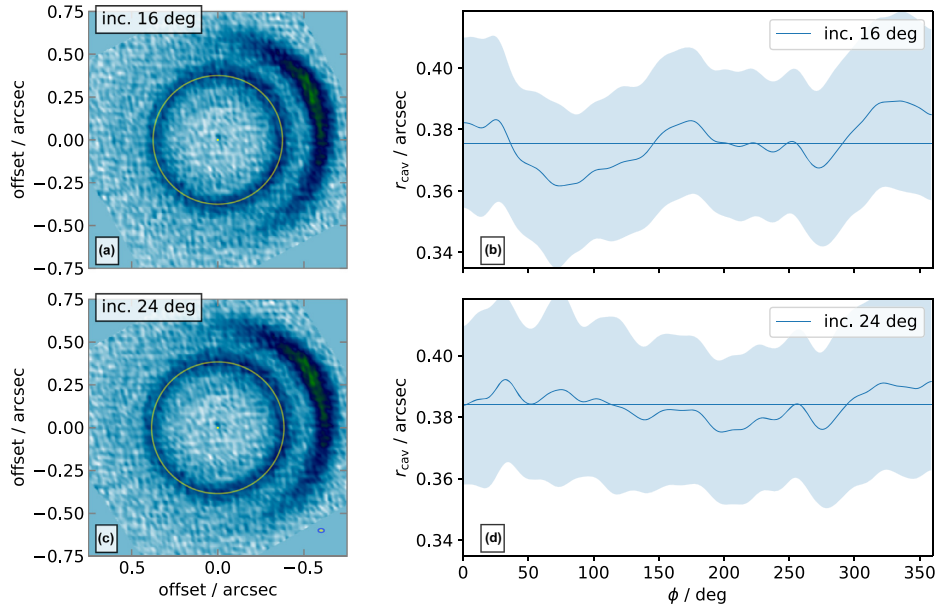
Figure 5. (a) face-on view of the Briggs $r = 0$ image from Fig. 1b, assuming an inclination of 16 deg. (b) the azimuthal profile of the Gaussian centroid and dispersion in the inner ring, in a polar expansion of the image in (a), after smoothing over two beam major axis (the total height of the shaded area corresponds to 1σ). (c) and (d) same as (a) and (b), for the optimal orientation of 24 deg.

reduced this SPHERE/IRDIS data set with the IRDAP pipeline (van Holstein et al. 2020) to produce the image shown in Fig. 4a. We see in Fig. 4b that the contours that trace the Q_ϕ image come very close to the (possible) radio-millimeter filament. While we leave a detailed comparison between the filament and the spiral arms to Section 3.2, Fig. 4b shows another interesting similarity between the radio-millimeter and IR in this source. The faint continuum pedestal abut inside the inner ring appears to surround the bright inner ring in polarized intensity. Such faint pedestals are also seen in other systems, as, for example, in the rings of DoAr 44 and RXJ 1633.9 (called inflection points in Cieza et al. 2021) and in PDS 70 (Isella et al. 2019).

The continuum images can be used to infer disc orientation. We minimized the scatter in the radial profile, extracted by averaging in azimuth over the radial range [0″.25, 0″.45] (so enclosing only the inner ring). The procedure involves four free parameters: the disc position angle (PA), inclination i, and the origin for the polar expansions, which is offset relative to the origin of coordinates in the images by $\Delta\alpha$ in right-ascension and $\Delta\delta$ in declination. We used the MPOLARMAPS package, which is described in appendix. The posterior distributions were sampled with the EMCEE package (Foreman-Mackey et al. 2013), using flat priors. The disc orientation resulting from the tclean image with $r = 0$ Briggs weights is PA $= 241.6^{+6.9}_{-6.0}$ deg, $i = 23.80^{+2.5}_{-2.6}$ deg, $\Delta\alpha = 2^{+3}_{-4}$ mas, $\Delta\delta = 12^{+4}_{-4}$ mas. The origin of the polar expansion is plotted with a red marker in Fig. 1. We note that the disc PA is consistent with that used by Cazzoletti et al. (2018), considering that here we point PA at the position of the ascending node, but the disc inclination inferred in this work is significantly higher. The face-on views in Fig. 5 show that the present inclination results in a circular inner ring, albeit offset from the central emission. The orientation that corresponds to the most axially symmetric ring results in a scatter for the azimuthal profile of the ring radius of $\sigma(r_{\mathrm{cav}}) = 5$ mas about a median of 0″.38. However, a lower inclination of $i = 16$ deg results in a pronounced eccentricity in the deprojected (face-on) views, which is more conspicuous in the

polar expansions, with an azimuthal scatter $\sigma(r_{\mathrm{cav}}) = 8$ mas, about a median of 0″.37.

The high inclination resulting from the present analysis of the continuum may reflect that the inner ring is intrinsically eccentric. As discussed below (Section 3.4), an inclination close to $i = 16$ deg is required to bring the dynamical mass of the star in agreement with photospheric measurements. The difference with the inferred inclination of $i = 23.80^{+2.5}_{-2.6}$ deg based on the inner dust ring suggests that the inclination difference, of $\sim 7.8 \pm 2.5$, is due to intrinsic ring eccentricity, which corresponds to $e = 0.14 \pm 0.04$. This value is comparable to the measurement of $e \sim 0.1$ in MWC 758 by Dong et al. (2018a).

The difference in the continuum inclination derived here with the lower values reported in Cazzoletti et al. (2018), might be due to their use of a parametric model that results in large visibility residuals. In their noisiest data, those from ALMA Band 3, the residuals are adequately thermal and the inclination is $i = 17.7^{+3.4}_{-4.7}$ deg, so consistent with our value of $i = 23.80^{+2.5}_{-2.6}$ deg given the error bars. However, their value with the smallest errors, of $i = 9.8 \pm 0.1$ deg in Band 7, results in non-thermal residuals suggesting that the parametric model does not provide a good fit and that these uncertainties are thus artificially low. Another possible source of discrepancy is that Cazzoletti et al. (2018) kept the disk position angle fixed in their optimization, thereby reducing the uncertainties on inclination. Whichever the source of the bias, an inclination of $i = 9.8 \pm 0.1$ deg would yield much too high dynamical stellar masses (see Section 3.4).

3.2 Spiral arms

Both the native and tapered versions of the velocity-integrated ^{12}CO(2-1) intensity map $I_{\mathrm{Gauss}}(^{12}\mathrm{CO}(2\text{-}1))$ and its dispersion $\sigma_v(^{12}\mathrm{CO}(2\text{-}1))$ reveal a double-armed spiral pattern (Figs 2 and 3), reminiscent of the morphology of the near-IR spirals reported in Muto et al. (2012), Stolker et al. (2016). In order to facilitate

the interpretation of these spirals, we identified their trace in both $I_{\text{Gauss}}(^{12}\text{CO}(2\text{-}1))$ and the H−band Q_ϕ image, fitted these traces to different spiral equations, and compared the best-fitting models with $I_{\text{Gauss}}(^{12}\text{CO}(2\text{-}1))$, the H−band image (hereafter the IR image) and the sub-millimeter continuum image (Fig. 6).

We first identified local radial maxima in 1-deg wide slices in the *uv*-tapered $I_{\text{Gauss}}(^{12}\text{CO}(2\text{-}1))$ (where the spirals are the most conspicuous), after subtraction of the median radial intensity profile. These median intensities are integrated azimuthally over concentric 1-FWHM wide ellipses for all pixels, considering the mid-plane orientation of the disc inferred from the CO rotation curves (Section 3.3; $i \sim 16$ deg and PA ~ 241.9 deg). In each azimuthal slice, the vicinity of each radial maximum identified is then fitted to a 1D Gaussian profile using SCIPY's `curve_fit` routine. For each position angle, the radial separation and associated uncertainty on the spiral trace are set as the centroid of the Gaussian, and the maximum between the uncertainty on the centroid and half the beam size of our observations, respectively. The traces inferred with this procedure are shown as cyan crosses in Fig. 6a. We then fitted these traces to the equation of a general Archimedean spiral ($r = a + b\theta^n$), and found the best-fitting parameters using SCIPY's Nelder-Mead minimization algorithm. Since the objective of this fit is the comparison of the CO spirals with the IR spirals, we did not deproject the disc, hence the choice for a general Archimedean spiral equation for the fit.

We then proceeded to a similar analysis in IR image from Section 3.1 (Fig. 4). The southwest spiral shows a sudden discontinuity in pitch angle, identified as 'kink' in Muto et al. (2012) and Stolker et al. (2016). They attributed the kink to the location of a planet driving this spiral arm, which they labelled 'S1'. Therefore we adopted a different equation for the fit of this specific spiral trace. Instead of a general Archimedean spiral, we considered the expected shape from a spiral density wave excited by an embedded planet in the linear or weakly non-linear regime (Rafikov 2002):

$$\theta(r) = \theta_p + \frac{\text{sign}(r - r_p)}{h_p}$$
$$\times \left\{ \left(\frac{r}{r_p}\right)^{1+\beta} \left[\frac{1}{1+\beta} - \frac{1}{1-\alpha+\beta}\left(\frac{r}{r_p}\right)^{-\alpha}\right] - \left(\frac{1}{1+\beta} - \frac{1}{1-\alpha+\beta}\right) \right\} \quad (3)$$

where (θ_p, r_p) are the polar coordinates of the planet location, h_p is the disc aspect ratio at the planet's location, and α and β are the exponents of power laws for the angular frequency of the disc ($\Omega \propto r^{-\alpha}$) and the sound speed ($c_s \propto r^{-\beta}$), respectively. The five parameters of this equation are known to be highly degenerate (e.g. Muto et al. 2012; Christiaens et al. 2014). Furthermore, the linear or weakly non-linear approximation is only valid in the vicinity of the planet (e.g. Zhu et al. 2015), with an increasingly larger pitch angle (with respect to the linear approximation) the further the separation with the planet location. Given these considerations, we restricted the spiral trace to only a section subtending 45 deg around the twist. Moreover, we fixed α to 1.5 (Keplerian rotation) and β to 0.207, the average flaring found in Avenhaus et al. (2018) based on their sample of H-band polarized intensity images of protoplanetary discs, and left θ_p, r_p and h_p as free parameters. Since equation (3) assumes a face-on view of the disc, we deprojected the near-IR image using DISKMAP[4] (Stolker et al. 2016), adopting $\beta = 0.207$ and an initial estimate of 0.1 for h_p. We also scaled the image by r^2 to compensate for stellocentric flux

dilution. We then proceeded with finding the optimal values of θ_p, r_p and h_p with SCIPY's Nelder-Mead minimization algorithm, iteratively updating the value of h_p used for the disc deprojection. The values of h_p used for deprojection and found by the fit of the spiral traces converged to within 0.1 per cent relative values within two iterations. The final values we inferred are a PA of 212.4 ± 0.7 deg and $r = 425.9 \pm 1.2$ mas (57.8 ± 0.2 au) for the planet's location, and a disc aspect ratio $h_p = 0.017 \pm 0.001$ at that location, at the epoch of the IRDIS observations. The uncertainties on each parameter were found by bootstrapping (1000 bootstraps). We tested different values of β ranging from 0 to 0.25 and found consistent values of θ_p, r_p and h_p. Fig. 6b shows the best-fitting model on to the deprojected disc image, with intensities scaled by r^2. We notice a tentative radial shift between the CO models and IR spirals, which is likely due to the different emitting and scattering surfaces for $^{12}\text{CO}(2\text{-}1)$ and sub-micrometer-sized dust grains, respectively (e.g. Pinte et al. 2018; Avenhaus et al. 2018).

The best-fitting disc aspect ratio for the scattering surface, $h_p = 0.017 \pm 0.001$ appears significantly smaller than the expected value based on the $^{12}\text{CO}(2\text{-}1)$ brightness temperature ($h_g \sim 0.1$, see Section 3.3 and Fig. 8d). One possibility to account for both the very low inferred value of h_p for the IR spiral fit and the small apparent radial shift between the IR twist and the sub-millimeter continuum filament is that the outer spiral arm (with respect to the twist) is more curled-in towards the star at the H-band scattering surface than the inner spiral (as e.g in the 3D simulations of Zhu et al. 2015). This may result from a geometrically thick and vertically non-isothermal disk (i.e. non-constant sound speed at a given cylindrical radius). Alternatively, if the spiral structure traces surface waves, it may also travel slower than sound speed, hence inducing more tightly wound spirals than predicted by the spiral density wave theory. Since the value of h_p inferred in the fit depends on the apparent radial amplitude of the twist, a more curled in outer spiral would artificially reduce the inferred value of h_p. Furthermore, this curling-in would also explain the radial shift between the outer part of S1 and the azimuthal asymmetry in the outer sub-millimeter continuum ring. The latter appears to be located in the continuity of the filament, and it may thus be tracing dust following the gas density enhancement in the planetary wake, which may be possible for low Stokes number (see e.g. Veronesi et al. 2019). In this scenario, the spiral wake models of equation (3) (as used in Fig. 6) would suggest a mid-plane temperature of the order of ∼25 K ($h_p \sim 0.07$) to follow the pitch angle of the candidate filament and join the outer ring. It is worth noting however that the radial dependence of the sound speed (and hence the temperature profile) is assumed to be a power law in the derivation of equation (3), with a constant power index equal to $-\beta$. Therefore, if the sound speed (or more broadly the wave propagation speed) follows a more complex radial profile, the spiral morphology would deviate accordingly and would possibly follow more closely the shape of the outer ring asymmetry.

Finally, we compared all spiral models to our sub-millimeter continuum image of the disc (Fig. 6c). Taking into account Keplerian rotation around a star with mass $M_\star = 1.67^{+0.18}_{-0.16}M_\odot$ (Wichittanakom et al. 2020), and for a distance of 135.7 ± 1.4 pc (Gaia Collaboration 2018), the difference of 3.04 yrs Muto et al. (2012) between the epochs of the IRDIS and ALMA data corresponds to a prograde rotation of ∼3.7 deg. amount in the right panel of Fig. 6. More precisely, we used the deprojected IR model (shown in the middle panel of Fig. 6) for the rotation and subsequent re-projection on to the disc mid-plane (i.e. considering the inclination of the disc, but not the original flaring) – see left panel of Fig. 6 for the relative locations of the non-deprojected spiral model with respect to the filament.
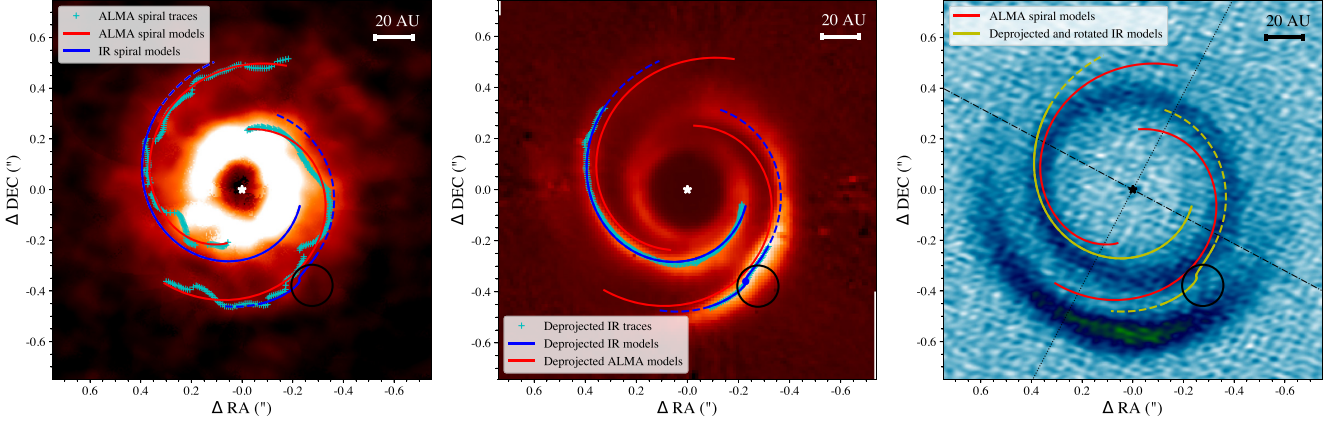
[4] https://github.com/tomasstolker/diskmap

Figure 6. Spiral traces (cyan crosses) identified in the velocity-integrated ^{12}CO(2-1) intensity map $I_{Gauss}(^{12}CO(2-1))$ and the near-IR scattered-light image, and corresponding best-fitting spiral models compared to $I_{Gauss}(^{12}CO(2-1))$ (left), the deprojected near-IR scattered-light image (middle) and the sub-millimeter continuum image (right). The location of the gap-crossing sub-millimeter continuum filament is circled in all panels. All images are shown in linear scale, with cuts corresponding to the 5th and 95th percentiles of pixel intensities for the ^{12}CO(2-1) moment 0 map, and min/max cuts for the IR and continuum images. The IR spiral models are shown projected (i.e. as observed) in the left panel, and deprojected on to the plane of the sky (i.e. after flaring and inclination correction) in the middle panel. The best-fitting location of the planet for the fit to equation (3) is provided with a blue dot in the middle panel. In the sub-millimeter continuum image, the deprojected model for the south-west IR spiral is rotated by 3.7 deg in the prograde direction, and subsequently projected on to the disc mid-plane (i.e. considering disc inclination, but not surface flaring). The semi-major and semi-minor axes are shown with dotted-dashed and dotted lines, respectively.

This angular shift of 3.7 deg nicely aligns the PA of the tentative filament ($\sim$216.1 deg; Section 3.1) and that of the IR spiral arm twist (216.1 ± 0.7 deg after rotation). However, we measure a radial shift $\gtrsim 42.1 \pm 1.2$ mas between the centre of the filament ($\sim$468 mas) and the planet location inferred from our fit to the IR twist, even after deprojection. The ALMA pointing uncertainty appears insufficient to account for this radial shift, as it is $\lesssim 15$ mas, e.g. if the sub-millimeter continuum signal near the centre of the cavity is tracing the star (see inset of Fig. 1a). As mentioned above, the observed radial shift may be consistent with the expected curling of the spiral wave towards the star (e.g. Zhu et al. 2015) as the IR scattering surface would be located at a shorter deprojected radius than the bulk of the density wave (in the mid-plane and likely consistent with the locus of the continuum filament). It is worth noting that given the likely eccentric geometry of the inner ring (Section 3.1), the planet may also be on a slightly eccentric orbit, which may also partially contribute to this offset.

3.3 Line diagnostics of physical conditions

The uniform slab approximation goes a long way in observational astronomy, as it is a simple means to extract physical conditions in a given line-of-sight. We use this approximation to estimate physical conditions in the gas using the CO isotopologue rotational lines. In local-thermodynamic-equilibrium (LTE) the emergent intensity from ground-state rotational lines depends on the column of the emitting specie, on the uniform-slab temperature T_b, and on the line-of-sight turbulent broadening v_{turb}. We write the gas temperature with an under-script 'b' to remind that, in the case of CO, this temperature is close to the brightness temperature of the optically thick ^{12}CO. Given fractional abundances, the emitting column can be converted into a total gas surface density, Σ_g. We have developed a tool to fit multi-isotopologue data with these free parameters, which we call SLAB.LINE. Related approaches have also been considered by others (Teague et al. 2016; Flaherty et al. 2020; Garg et al. 2020; Yen & Gu 2020). The model line profile for a given line of sight $\vec{x}$ is

$$I_\nu^m(\vec{x}) = B_\nu(T_b(\vec{x}))[1 - \exp(-\tau_\nu(\vec{x}))], \tag{4}$$

as a function of frequency ν, with

$$\tau_\nu(\vec{x}) = \kappa_L(\vec{x})\Sigma_g(\vec{x})f_{mol}\Phi_\nu(\vec{x}). \tag{5}$$

The line opacity $\kappa_L(\vec{x})$ is approximated in LTE, so for a rotational transition $J_2 \rightarrow J_1$

$$\kappa_L(\vec{x}) = \frac{h\nu_\circ}{4\pi m_{H_2}} \frac{g_{J_1}e^{-\frac{E_{J_1}}{kT_b(\vec{x})}}}{Z(\vec{x})} B_{12} \left[1 - e^{-\frac{h\nu_\circ}{kT_b(\vec{x})}}\right]. \tag{6}$$

We use the LAMDA molecular database (Schöier et al. 2005), and evaluate the partition function $Z = \sum_{J=0}^{J_{max}} g_J e^{-\frac{E_J}{kT_b}}$ by summing over all tabulated rotational energy levels E_J (so for ^{12}CO this corresponds to $J_{max} = 40$). In equation (5), f_{mol} is the abundance by number of the emitting molecule relative to H_2. In this case for the CO isotopologues we set $f_{^{13}CO} = \frac{1}{76}f_{^{12}CO}$ (from Casassus, Stahl & Wilson 2005; Stahl, Casassus & Wilson 2008), $f_{C^{18}O} = \frac{1}{500}f_{^{12}CO}$ (Wilson & Rood 1994), with $f_{^{12}CO} = 10^{-4}$. The line profile is simply a thermal Gaussian broadened by turbulence, with dispersion $v_{turb}(\vec{x})$ and velocity centroid $v_\circ(\vec{x})$:

$$\Phi_\nu(\vec{x}) = \frac{1}{\sqrt{2\pi}\sigma_{v_\circ}} \exp\left(-\frac{(\nu - \nu_\circ)^2}{2\sigma_{v_\circ}^2}\right), \tag{7}$$

with $\nu_\circ = \frac{E_{J_2}-E_{J_1}}{h}(1 + \frac{v_\circ}{c})$ and

$$\sigma_{v_\circ}(\vec{x}) = \frac{\nu_\circ}{c}\sqrt{\frac{kT_b(\vec{x})}{m_{mol}} + v_{turb}^2(\vec{x})}, \tag{8}$$

and where m_{mol} is the molecular mass.

The free parameters $v_\circ$, Σ_g, T_b and v_{turb} were constrained in each line of sight $\vec{x}_l$ independently with a least-squares fit to the observed spectra in the three isotopologue transitions:

$$\chi^2(\vec{x}_l) = \sum_{i=1}^{3} \frac{1}{I_{rms,i}^2(\vec{x}_l)} \sum_{v_k} (I_{v_k}(\vec{x}_l) - I_{v_k}(\vec{x}_l)^m)^2, \tag{9}$$

where the sum in frequencies $\{v_k\}$ runs over all available spectral channels. The noise in each line of sight, $I_{rms,i}(\vec{x}_l)$, is taken as the rms dispersion in the observed spectra ± 1 km s^{-1} away from the peak of
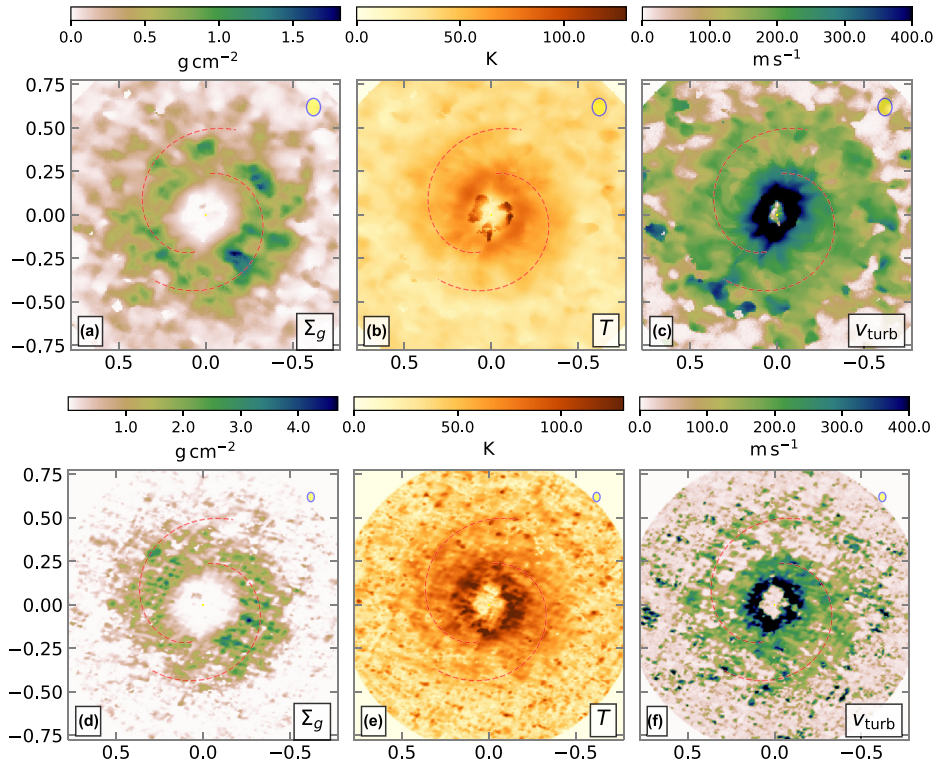
Figure 7. Example application of SLAB.LINE to extract physical conditions in HD 135344B using the ^{12}CO(2-1), ^{13}CO(2-1) and C^{18}O(2-1) lines.a,b,c: measurements inferred from the *uv*-tapered datacubes. (a): total gas surface density Σ_g, (b): gas temperature T_b, (c): turbulent line broadening $v_{\rm turb}$. (d,e,f): same as a,b,c but for the original datacubes without *uv*-tapering. The dashed red lines corresponds to the traces of the CO spirals obtained in Section 3.2.

the line. The optimization for each line of sight was carried out in the logarithm of the positive-definite parameters, i.e. the full set of parameters is $(\log_{10}(\Sigma_g), \log_{10}(T_b), v_\circ, \log_{10}(v_{\rm turb}))$. An application of the conjugate-gradient method, as implemented in SCIPY.OPTIMIZE, yielded a first approximation to adequate sets of parameters. We then sampled parameter space with the emcee package (Foreman-Mackey et al. 2013), which is a Markov chain Monte Carlo ensemble sampler (Goodman & Weare 2010), using flat priors.

An application of SLAB.LINE to HD 135344B is shown in Fig. 7, where we report the fields for $\Sigma_g(\vec{x})$, $T_b(\vec{x})$ and $v_{\rm turb}(\vec{x})$ inferred from both the natural-weights datacubes and the $uv-$tapered datacubes. These fits assumed fixed isotopologue abundances, but we reach thermal residuals none the less. We refer to Appendix C for a discussion of goodness of fit, correlation analysis, and example lines of sights.

In Fig. 7 it is particularly interesting to note the similarity between $v_{\rm turb}$ and the line velocity dispersion map $\sigma(\vec{x})$ in Figs 2 and 3, as both follow the spiral pattern discussed in Section 3.2, but Σ_g and T_b do not. The larger scale spiral is best traced in the *uv*-tapered version of $v_{\rm turb}(\vec{x})$, while the root of the spirals is seen in the native version (with no *uv*-taper).

Another interesting feature of the line diagnostics in Fig. 7 is the absence of a local peak neither Σ_g nor T at the position of the filament. This is surprising because this position coincides with the maximum line intensity in ^{18}CO(2-1) (see Section 2). A possible interpretation is that the mid-plane near the candidate is hotter than the surface sampled in ^{12}CO(2-1).

The large continuum crescent in the outer ring, at $\sim$80 au or $\sim$0′′.6, is absent from the $\Sigma_g(\vec{x})$ map in Fig. 7 (and also from the azimuthal averages in Fig. 8). This may seem surprising in the context of the

dust trap interpretation, since the required local pressure maximum should correspond to a local peak in Σ_g (Birnstiel et al. 2013, even if this local peak can be quite shallow). However, a similar result is seen in MWC 758, where the position of the dust peak does not correspond to a maximum in Σ_g, as inferred from the CO isotopologues (Boehler et al. 2018). In HD 135344B, while it appears that the CO mass surface density is fairly homogeneous across the disc, it may be that the CO(2-1) isotopologues come short of reaching deep enough to sample the total mass surface density. This could result from freezing of CO on to dust grains, or because the continuum is optically thick, so that thermal equilibrium between dust and gas in the denser regions would leave no net line emission after continuum subtraction (see Boehler et al. 2017, for a detailed description of this effect).

The radial profiles for Σ_g and T_b, obtained with azimuthal averages and a disc inclination of $i = 16$ deg, are shown in Figs 8b and 8c. The CO line temperatures reach close to $\sim$115 K, which would be the dust temperature for water condensation, out to $\sim$25 au. Within $\sim$20 au, confusion of different Keplerian velocities in the finite beam exaggerate the turbulent velocities along an inner ring inset within the hot inner ring seen in T_b, which is itself inset within the dense ring seen in Σ_g. The lack of signal inside the ^{12}CO central cavity (within 0′′.1) yields spuriously low values for T_b because we have set a maximum value for T_b of $3\times$ the peak line brightness temperature (see Section C). Note that releasing this upper limit on T_b yields somewhat higher temperatures and somewhat lower values for $v_{\rm turb}$ inside the central cavity, but also leads to glitches in T_b in the outer regions (albeit with little impact on the other parameters). The best-fitting TING values for T_b come close, at $\sim$−30 per cent, of the radial temperature profile of the $\tau = 1$ surface in the ^{12}CO(2-1) line as estimated from detailed thermochemical modelling of the (3-2)
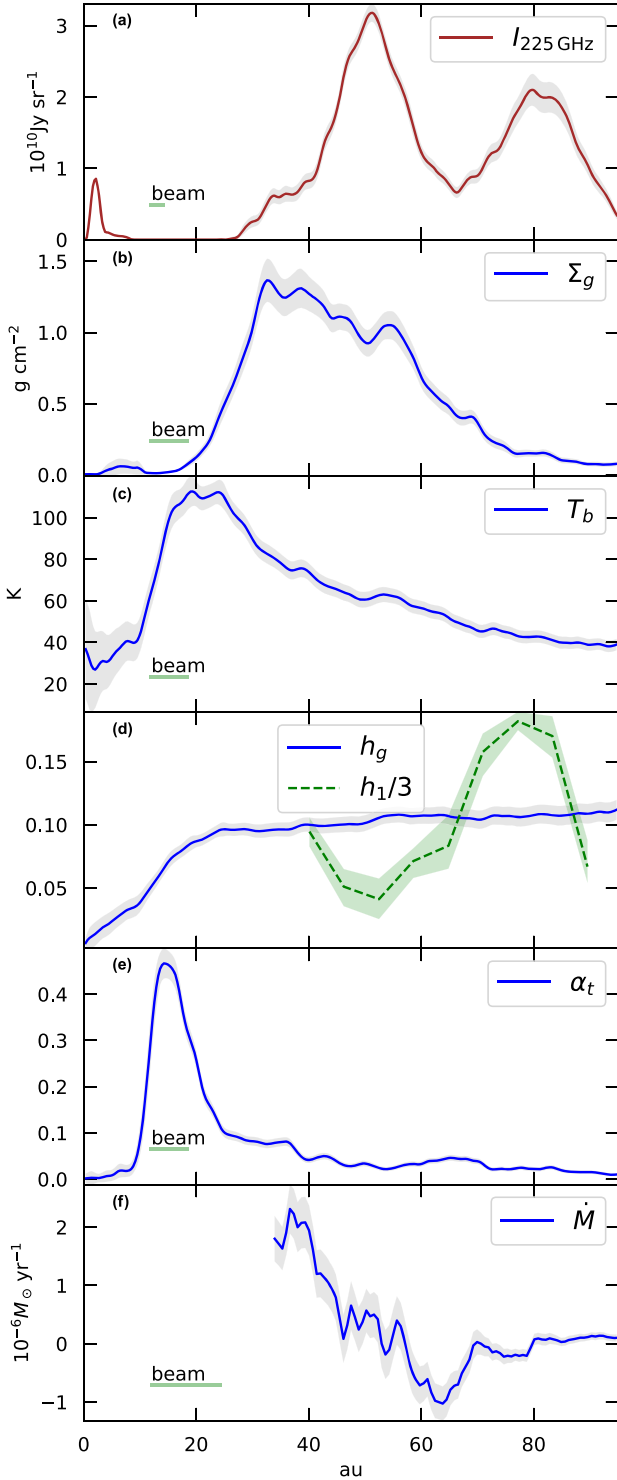
Figure 8. Radial continuum intensity profile and properties of the HD 135344B inferred from the uniform slab diagnostics with SLAB.LINE and from the disc rotation curve: (a) Azimuthal average of the 225 GHz continuum intensity profile extracted from the image in Fig. 1c. (b) gas surface density profile $\Sigma_g(R)$, (c) gas temperature profile $T_b(R)$, (d) aspect ratio profile $h_g(R) = c_s/\Omega_K$, and comparison with the unit-optical-depth surface $h_1(R)$, (e) turbulence parameter $\alpha_t = (v_{\mathrm{turb}}/c_s)^2$, f) accretion rate $\dot{M}(R) = -2\pi R \Sigma_g \tilde{v}_R$.

CO isotopologue lines (DALI model in van der Marel et al. 2016a). In Fig. 8c, T_b appears to be above the CO sublimation temperature of ∼20 K everywhere in the CO layer. However, colder CO in the midplane could have condensed on the dust grains, where the gas phase CO abundance is much lower ($f_{12\mathrm{CO}} \sim 10^{-12}$, van der Marel et al. 2016a). This is reflected in the factor of ∼10 larger gas surface density derived from the CO(3-2) isotopologues with DALI. The SLAB.LINE diagnostics thus yield a lower limit to the total gas mass, since in general $f_{12\mathrm{CO}} < 10^{-4}$. The global structure of $\Sigma_g(R)$ inferred from SLAB.LINE is consistent with previous estimates based on parametric modelling, either with the location of the sharp gas cavity edge placed at 30 au by van der Marel et al. (2016a), or with the gradual density drop inwards used by van der Marel et al. (2021), with a gap at ∼20 au.

The lack of ^{12}CO integrated intensity at the centre of the cavity is suggestive of a very low column density of ^{12}CO, and is reflected in the value of Σ_g near the star, which is consistent with zero. This central hole could be caused by photo-dissociation driven by UV irradiation. The ^{12}CO integrated intensity is so low in the disc's innermost regions that photo-dissociation could act down to the disc mid-plane. For this to happen, gas surface densities $\lesssim 10^{-2}$ g cm^{-2} are necessary (see, e.g. equation 4 of Baruteau et al. 2021 for $z = 0$). Interestingly, the modelling of CO ro-vibrational observations by Carmona et al. (2014) indicates that the gas surface density in the cavity of the HD135344B should be $\lesssim 10^{-2}$ g cm^{-2} (see the lower-right panel in their Fig. 6), which would support the idea that photo-dissociation could indeed be responsible for the lack of ^{12}CO integrated intensity inside the cavity.

3.4 Rotation curve

The rotation curve can be extracted from the velocity centroid map and brings constraints on the central (stellar) mass and orientation (Casassus & Pérez 2019). From the observations presented in Section 2, the velocity field of the top layer in ^{12}CO(2-1) is best traced with the double-Gaussian moments applied to either the UVMEM-restored or the *uv*-tapered datacubes. For conciseness we choose to report on the *uv*-tapered version, as it allows an extension to larger radii and is consistent with the results from the finer angular resolutions, even at radii as small as 0″.25.

The 3D rotation curve $\vec{\tilde{v}}(R) = (\tilde{v}_R(R), \tilde{v}_\phi(R), \tilde{v}_z(R))$, in disc-centred cylindrical coordinates where $z = 0$ coincides with the mid-plane, also informs on large-scale radial and vertical flows (Teague, Bae & Bergin 2019). We extended the same procedure as described in Casassus & Pérez (2019) to 3D in the CONEROT package.[5] In an axially symmetric disc the unit opacity surface in an optically thick line such as ^{12}CO(2-1) can be represented by its height over the mid-plane, $h_1(R)$. We approximate this surface by a series of cones whose orientations are fit to the observed velocity centroid in concentric radial domains, or 'regions', which we combine by averaging as described in Casassus & Pérez (2019). The procedure is similar to that followed by the EDDY package (Teague et al. 2019), except that the disc orientation along with the rotation curve are both optimized to fit v_1° in each region.

A full optimization to fit v_1° over the radial domain [0″.3, 0″.7], with an axially symmetric model in a purely azimuthal flow and varying the disk orientation, results in loose constraints on the disk inclination. In initial trials, we used the tclean datacubes, *uv*-tapered to a 0″.12 beam, and obtained $i = 17.6^{+2.7}_{-3.2}$ deg, PA $= 241.9^{+0.4}_{-0.5}$ deg, and

---

[5] publicly available at https://github.com/simoncasassus/ConeRot

an aspect ratio $h_1 = 0.28^{+0.06}_{-0.05}$ (for the unit-opacity surface), and a systemic velocity $v_{\rm lsr} = 7.12 \pm 0.02\,{\rm km\,s^{-1}}$ (see Casassus & Pérez 2019, for details). When using the definitive data set, based on the UVMEM reconstructions (so with a 20 per cent narrower beam at the expense of slightly noisier maps), we obtain $i = 23.4^{+2.0}_{-6.2}$ deg, PA $= 242.4^{+0.6}_{-0.7}$ deg, $h_1 = 0.27^{+0.19}_{-0.08}$ and $v_{\rm lsr} = 7.10 \pm 0.02\,{\rm km\,s^{-1}}$.

We therefore opted to fix the inclination to $i = 16$ deg, which yields dynamical stellar masses that are consistent with the photospheric data (Wichittanakom et al. 2020, see below in this Section), and set PA $= 241.9$. We then proceeded to optimize the aspect ratio and the rotation curve in 11 radial bins over $[0.''25, 0.''75]$, which produced the 3D rotation curve shown in Fig. 9. The sign convention we follow is such that $\tilde v_z > 0$ and $\tilde v_R > 0$ points away from the disk mid-plane and from the star, as in an outflow. A face-on view of the disc using this geometry is shown in Fig. 10. The deviations from the axially symmetric flow appear to be thermal, although more pronounced in the region around the possible filament seen in the continuum. Deeper data are required to discuss these velocity deviations.

The dynamical stellar mass, fit to the tangential component $\tilde v_\phi(R)$, is $1.67 \pm 0.04 < M_\star/M_\odot < 1.89 \pm 0.04$. The lower limit stems from assuming perfect cylindrical rotation, while the upper limit corresponds to Keplerian vertical shear. This stellar mass is consistent with that measured from the photospheric spectrum (Wichittanakom et al. 2020), $M_\star = 1.67^{+0.18}_{-0.16}M_\odot$.

In a rotation curve fit, the resulting stellar mass is quite sensitive on inclination i:

$$M_\star \propto R \times \tilde v_\phi^2(R) \propto \frac{1}{\cos(i)} \times \frac{1}{\sin^2(i)}, \qquad (10)$$

if the extracted rotation curve and disk aspect ratio are kept equal (aside from the $\sin(i)$ factor). For comparison, if we fix $i = 24$ deg (as inferred from the continuum), an application of CONEROT gives $0.91 \pm 0.04 < M_\star/M_\odot < 0.98 \pm 0.04$ (the lower limit would be $0.92\,M_\odot$ in an extrapolation of the stellar mass value from $i = 17.6$ deg using equation 10). In turn, if we fix inclination to 9.8 deg, the measurement with the smallest error bars in Cazzoletti et al. (2018, their Band 7 case), then $4.9 \pm 0.04 < M_\star/M_\odot < 6.8 \pm 0.04$ (the lower limit from equation (10) would be $4.9\,M_\odot$).

If the tentative sub-millimeter continuum filament traces a planetary wake, one may expect the planet in the sub-millimeter annular gap to also carve a dip in the gas surface density, whose signature may be observable in ^{12}CO if the planet is massive enough. The opening angle of the cone tracing the ^{12}CO(2-1) unit opacity surface corresponds to an aspect ratio of $h_1 \sim 0.1$ at $\sim 0.''4$ separation (i.e. in the sub-millimeter annular gap), compared to $h_1 > 0.2$ beyond the annular gap (see Fig. 9).

4 DISCUSSION

As noted in Section 2, the same two-armed grand-design spiral that characterizes the near-IR scattered-light images also stands out in the ^{12}CO(2-1) velocity-integrated intensity and in the line velocity dispersion (or second-order moment). However, the spiral pattern is absent in the peak intensity map (Fig. 2). The absence of a counterpart in peak intensity suggests that the spiral structure is not due to a local enhancement in temperature, but is instead due either to a strong modulation in gas surface density, or to enhanced velocity dispersion. The lack of a conspicuous spiral pattern in the rarer isotopologue maps, which are optically thinner, suggests that the spirals probably do not correspond to enhanced surface densities. These arguments tentatively support the case of 'turbulent spirals', i.e. that turbulence,
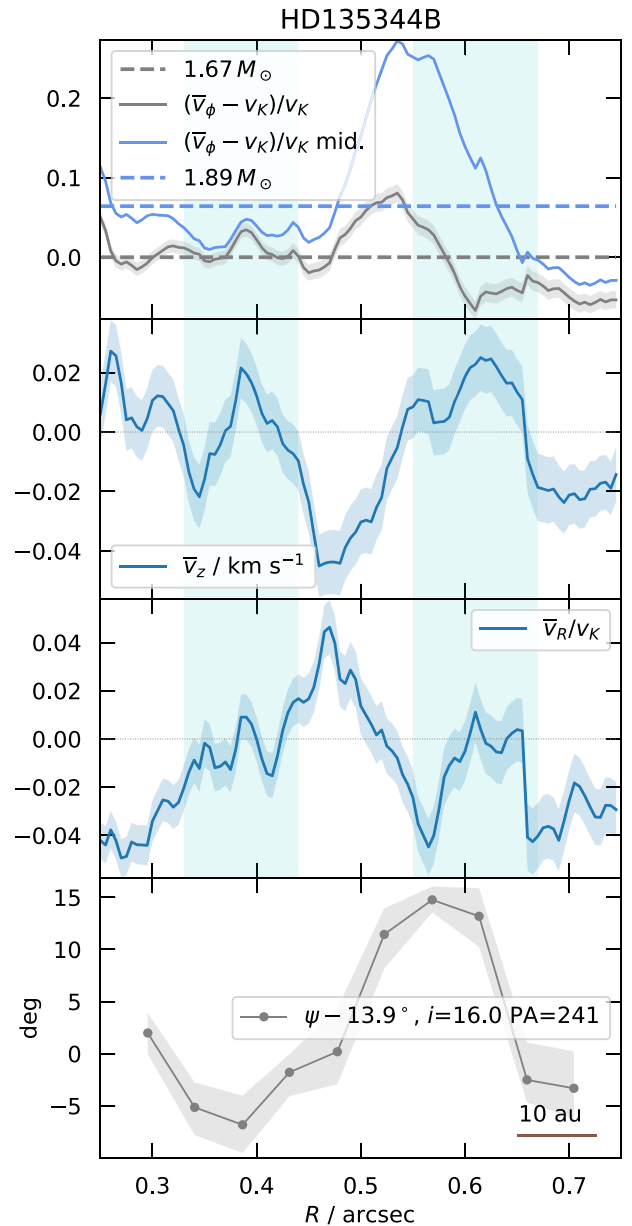

Figure 9. Rotation curve in HD 135344B. The regions in cyan correspond to the total extent of the two rings. From top to bottom, we show: (1) The azimuthal rotation curve $\tilde v_\phi(R)$. The dashed horizontal lines are comparison Keplerian profiles with the corresponding stellar mass. The curve labelled 'mid' is an extrapolation to the disc mid-plane assuming vertical Keplerian shear. (2) The vertical velocity component curve $\tilde v_z(R)$, where $\tilde v_z > 0$ points away from the disk mid-plane. (3) The radial velocity component $\tilde v_r(R)$, where $\tilde v_r > 0$ points away from the star. (4) The opening angle of the cone tracing the unit opacity surface for ^{12}CO(2-1).

or superposed velocity components along the line-of-sight, is strong in this disc and particularly so in the spirals.

The uniform-slab diagnostics obtained with SLAB.LINE show that the grand-design two-armed spiral in velocity-integrated intensity is neither seen in the gas surface density $\Sigma_g(\vec x)$ nor in the gas temperature $T_b(\vec x)$. Instead, it is reflected in the turbulent velocity map $v_{\rm turb}(\vec x)$. This is surprising as most attempts to constrain the level of turbulence in protoplanetary discs have resulted in upper limits,
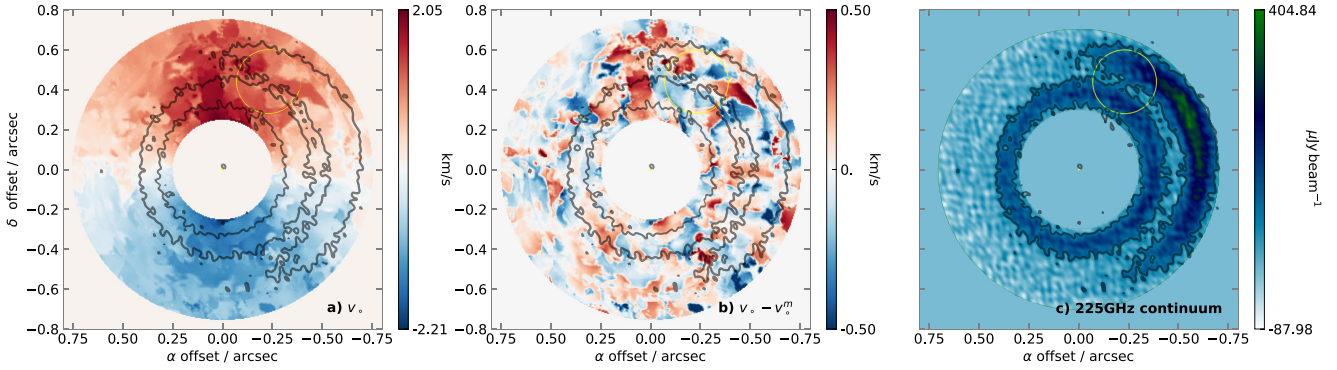
Figure 10. Face-on view of the kinematics in HD 135344B, inferred using CONEROT and the top-layer velocity centroid for the ^{12}CO(2-1) *uv*-tapered datacube. a) Deprojected velocity centroid (approximating the disc with a cone). The single contour traces the continuum image shown in (c), at 20 per cent peak. (b) Difference between the observed velocity field and the axially symmetric model, showing essentially thermal residuals. Deeper data are required to ascertain the structures seen near the position of the filament. (c) Comparison with a face-on view of the continuum, deprojected as a thin disc with inclination $i = 16$ deg. In all images the yellow circle highlights the position of the putative filament.

except in DM Tau (see Flaherty et al. 2020, and references therein), where values for $v_{\rm turb}$ are similar as reported here for HD 135344B.

In the α-viscosity model (Shakura & Sunyaev 1973) viscosity is related to the thermal disc structure by a dimensionless parameter, α_t. We can re-formulate our results by calculating this parameter locally, by comparing the turbulent velocities with the local sound speed, $\alpha_t \approx (v_{\rm turb}/c_s)^2$. The uniform-slab diagnostic yields the gas temperature $T_b(\vec{x})$, from which we obtain the sound speed $c_s = \sqrt{\gamma k_B T_b/(\mu m_p)}$, with an adiabatic index $\gamma = 1.4$ and a molecular weight $\mu = 2.3$. Fig. 8 shows that $\alpha_t(R)$ reaches values[6] of ~0.05.

The inferred values for α_t seem very high, especially in the vortex interpretation of the large crescent modulating the outer ring. This is because very low levels of 'alpha' viscosity, of order $\alpha \sim 10^{-4}$–10^{-3}, are necessary to develop the Rossby-wave instability and explain the outer ring crescent with an anticyclonic vortex (e.g. Barge & Sommeria 1995; Lyra & Lin 2013; Zhu & Stone 2014; Zhu & Baruteau 2016). The turbulent velocity map in HD 135344B is thus unlikely to actually trace the source of viscosity in the disc, but may instead reflect the superposition of several velocity components, or superposed laminar flows along the line of sight.

Interestingly, the rotation curve of HD 135344B points at strong accretion towards the star, especially inside the inner dust ring (so $<0\rlap.''4$). The radial velocity component, with a peak in absolute value $v_R = -0.34 \pm 0.05 \, {\rm km \, s^{-1}}$ (Fig. 9), comes close to the sound speed, which ranges from ~$0.64 \pm 0.05 \, {\rm km \, s^{-1}}$ to $c_s \sim 0.44 \pm 0.04 \, {\rm km \, s^{-1}}$ over the radial domain plotted in Fig. 8. Transonic velocities are theoretically expected in the cavity of transition discs where magnetized winds result from thermal (photoevaporative) winds threaded by magnetic field lines, which exert a torque on the gas remaining in the wind and drive accretion (Wang & Goodman 2017). The likelihood of photoevaporative winds and net poloidal fields in discs is theoretically established (e.g. Ercolano & Pascucci 2017, and references therein).

We can estimate the corresponding accretion rate with $\dot{M}(R) = -2\pi R \Sigma_g \tilde{v}_R$. As illustrated in Fig. 8f, the peak accretion rate is $\dot{M} = (2 \pm 0.1) \times 10^{-6} \, M_\odot \, {\rm yr^{-1}}$. This rate is 40 times larger than the stellar accretion rate of $5 \times 10^{-8} \, M_\odot^{-1}$ (Fairlamb et al. 2015), and would deplete the disc mass sampled by CO(2-1), or ~$1.6 \times 10^{-3} \, M_\odot$, in

~800 yr (the fraction of the material accreted by a potential planet inside the ring is small). It may be that the mass reservoir is not sampled by CO, but even a very massive disc, with $0.1 \, M_\odot$, would still be much too short lived. The system may, perhaps, be observed in a transient phase, or an important fraction of the material being accreted inside ~50 au will eventually be expelled in a wind.

A similar issue as the disc depletion timescale also arises with the diverging accretion rates near 50 au, so right on the inner dust ring (see Fig. 8f). Since the accretion rate is negative right outside the ring, and reaches ~$(-1 \pm 0.2) \times 10^{-6} \, M_\odot \, {\rm yr^{-1}}$ at ~60 au, a gap would quickly develop at the location of the ring.

Another solution to both the very high values for α_t, and the very high apparent accretion rate, is that accretion is restricted only to the surface layer, where the ^{12}CO(2-1) line originates. This would be a similar situation as that of meridional flows at the edges of a protoplanetary gap, but here in the case of the outer edge of the central cavity. The mid-plane, enclosing most of the disc mass, may instead be almost in pure azimuthal rotation, with at least a factor of 10 smaller radial velocity than in the surface so as to reconcile the disc accretion rate with the stellar accretion. If this is the case, then the origin of the line broadening would indeed be the superposition of laminar flows along the line of sight, rather than genuine turbulence. The possibility of a strongly decreasing gradient for the radial velocity component towards the mid-plane can be tested with an extension of the rotation curve analysis from Section 3.4 to deeper CO isotopologue data. Theoretical models indeed suggest that both in the case of MRI-driven or wind-driven accretion, the active (accreting) layer in discs is expected to be confined to the surface (e.g. Mohanty, Ercolano & Turner 2013; Bai 2016).

5 CONCLUSIONS

The HD 135344B disc is especially interesting in the context of planet–disc interactions. Here we reported on new ALMA observations, with unprecedented angular resolutions in this source. The data correspond to a partial delivery with about 1/10 of the total integration, but none the less reveal interesting aspects of this disc, whose statistical significance will be further assessed pending delivery of the full data set:

(i) A thin filament in the continuum image at 225 GHz crosses the gap between the outer and inner rings (Fig. 1). Although its median

---

[6]the steep rise towards the origin corresponds to the spurious inner ring in $v_{\rm turb}$ that is due to weak signal and confusion, as discussed in Section 3.3

intensity is at 4 times the noise level, confirmation of this filament requires a second epoch and deeper observations. The filament is found at the same location as the putative protoplanet proposed to be driving one of the spirals by Muto et al. (2012), and almost co-aligned with a local twist in the IR spiral arm (same PA but radially shifted; Fig. 6c). We suggest that the radial shift is due to the curling of the spiral towards the star at the disc surface (Zhu et al. 2015).

(ii) The ^{12}CO(2-1) velocity-integrated and dispersion maps trace the same spiral seen in scattered light, and characteristic of HD 135344B (see Figs 3, 2 and 6c). The CO spiral is modulating an extended disc, and its arm-inter-am contrast is much shallower than in the near-IR. It is not affected by shadowing from a possible tilted inner disc. The spiral pattern and extended disc are absent from the peak intensity map, suggesting that the origin of the line broadening is turbulence rather than a temperature wave.

(iii) The physical conditions and line-of-sight turbulent broadening v_{turb} inferred from the uniform-slab and LTE approximations confirm that the extended disc is axially symmetric in the surface density of the CO layer, while v_{turb} follows the IR spiral (Fig. 7).

(iv) The magnitude of v_{turb} in this disc is very large, and close to $\sim$22 per cent sonic. The corresponding viscosity is $\alpha_t \sim 0.05$ (Fig. 8e), which is much higher than standard values and suggests that the line broadening stems from superposed laminar flows rather than genuine turbulence.

(v) The disc rotation curve points at an inclination of $\sim$16 deg, which is consistent with estimates of the central star mass from the photospheric spectrum. If this inclination is correct, the inner ring in continuum emission is quite eccentric, with $e = 0.14 \pm 0.04$, as the inclination required to circularize it is $i = 23.8^{+2.5}_{-2.6}$ deg (Fig. 5).

(vi) If the gaseous disc is axially symmetric, then its 3D rotation curve (Fig. 9), including radial and vertical axially symmetric flows, points at strong accretion inside the inner dust ring, within $\sim$0$''$4, with a radial velocity of up to $v_R = -0.34 \pm 0.05\,\mathrm{km\,s^{-1}}$. The corresponding mass accretion rate is $\dot{M} = (2 \pm 0.2) \times 10^{-6}\,M_\odot\,\mathrm{yr^{-1}}$ (Fig. 8f), which may be reconciled with the $\sim$40 times lower stellar accretion rate if only the surface layers are undergoing accretion.

ACKNOWLEDGEMENTS

DATA AVAILABILITY

The full ALMA data set for project 2018.1.01066.S will be available on the ALMA archive, at the term of the proprietary period. Meanwhile, the reduced ALMA data underlying this article is available upon reasonable request to the corresponding author. The original analysis packages that sustain this work are publicly available at the following URLs: https://github.com/simoncasass us/GMoments https://github.com/simoncasassus/MPolarMapshttps://github.com/simoncasassus/ConeRot https://github.com/simoncasassus/Slab

AUTHOR CONTRIBUTIONS

S.C: imaging, analysis, write-up, telescope proposal, software development: GMOMENTS, MPOLARMAPS, CONEROT and SLAB.LINE. V.C.: telescope proposal, Section 3.2 on spiral fits. M.C.: UVMEM imaging and software development. S.P.: IRDAP reduction, telescope proposal. P.W., C.B., D.P: planet-disc hydrodynamical context. B.E.: disc-wind context. N.vdM.: literature on HD 135344B. R.D.: Estimate of ring eccentricity. A.J: advice on SLAB.LINE. All authors commented on the manuscript.

REFERENCES

ALMA Partnership et al., 2015, ApJ, 808, L3
Andrews S. M. et al., 2018, ApJ, 869, L41
Avenhaus H. et al., 2018, ApJ, 863, 44
Avenhaus H., Quanz S. P., Meyer M. R., Brittain S. D., Carr J. S., Najita J. R., 2014, ApJ, 790, 56
Bai X.-N., 2016, ApJ, 821, 80
Barge P., Sommeria J., 1995, A&A, 295, L1
Baruteau C., Zhu Z., 2016, MNRAS, 458, 3927
Baruteau C., Wafflard-Fernandez G., Le Gal R., Debras F., Carmona A., Fuente A., Rivière-Marichalar P., 2021, 505, 359
Birnstiel T., Dullemond C. P., Pinilla P., 2013, A&A, 550, L8
Boehler Y. et al., 2018, ApJ, 853, 162
Boehler Y., Weaver E., Isella A., Ricci L., Grady C., Carpenter J., Perez L., 2017, ApJ, 840, 60
Cárcamo M., Román P. E., Casassus S., Moral V., Rannou F. R., 2018, Astron. Comput., 22, 16
Carmona A. et al., 2014, A&A, 567, A51
Carrasco-González C. et al., 2019, ApJ, 883, 71
Casassus S. et al., 2013, Nature, 493, 191
Casassus S. et al., 2015, ApJ, 812, 126
Casassus S. et al., 2018, MNRAS, 477, 5104
Casassus S. et al., 2019, MNRAS, 483, 3278
Casassus S., Pérez S., 2019, ApJ, 883, L41
Casassus S., Stahl O., Wilson T. L., 2005, A&A, 441, 181
Casassus S., Cabrera G. F., Förster F., Pearson T. J., Readhead A. C. S., Dickinson C., 2006, ApJ, 639, 951
Cazzoletti P. et al., 2018, A&A, 619, A161
Christiaens V., Casassus S., Perez S., van der Plas G., Ménard F., 2014, ApJ, 785, L12
Cieza L. A. et al., 2021, MNRAS, 501, 2934
de Val-Borro M., Artymowicz P., D'Angelo G., Peplinski A., 2007, A&A, 471, 1043
Dong R. et al., 2018a, ApJ, 860, 124

Dong R., Hall C., Rice K., Chiang E., 2015, ApJ, 812, L32
Dong R., Najita J. R., Brittain S., 2018b, ApJ, 862, 103
Dullemond C. P. et al., 2018, ApJ, 869, L46
Ercolano B., Pascucci I., 2017, R. Soc. Open Sci., 4, 170114
Fairlamb J. R., Oudmaijer R. D., Mendigutía I., Ilee J. D., van den Ancker M. E., 2015, MNRAS, 453, 976
Flaherty K. et al., 2020, ApJ, 895, 109
Foreman-Mackey D., Hogg D. W., Lang D., Goodman J., 2013, PASP, 125, 306
Francis L., van der Marel N., 2020, ApJ, 892, 111
Gaia Collaboration et al., 2018, A&A, 616, A1
Garg H. et al., 2021, MNRAS, 504, 782
Garufi A., Quanz S. P., Schmid H. M., Avenhaus H., Buenzli E., Wolf S., 2014, A&A, 568, A40
Goodman J., Weare J., 2010, Commun. Appl. Mathem. Comput. Sci., 5, 65
Haugbølle T., Weber P., Wielandt D. P., Benítez-Llambay P., Bizzarro M., Gressel O., Pessah M. E., 2019, AJ, 158, 55
Isella A., Pérez L. M., Carpenter J. M., Ricci L., Andrews S., Rosenfeld K., 2013, ApJ, 775, 30
Isella A., Benisty M., Teague R., Bae J., Keppler M., Facchini S., Pérez L., 2019, ApJ, 879, L25
Jennings J., Booth R. A., Tazzari M., Rosotti G. P., Clarke C. J., 2020, MNRAS, 495, 3209
Koller J., Li H., Lin D. N. C., 2003, ApJ, 596, L91
Li H., Colgate S. A., Wendroff B., Liska R., 2001, ApJ, 551, 874
Lovelace R. V. E., Li H., Colgate S. A., Nelson A. F., 1999, ApJ, 513, 805
Lyra W., Lin M.-K., 2013, ApJ, 775, 17
Marino S., Casassus S., Perez S., Lyra W., Roman P. E., Avenhaus H., Wright C. M., Maddison S. T., 2015, ApJ, 813, 76
Mittal T., Chiang E., 2015, ApJ, 798, L25
Mohanty S., Ercolano B., Turner N. J., 2013, ApJ, 764, 65
Muto T. et al., 2012, ApJ, 748, L22
Muto T. et al., 2015, PASJ, 67, 122
Ohashi S. et al., 2020, ApJ, 900, 81
Pérez L. M., Isella A., Carpenter J. M., Chandler C. J., 2014, ApJ, 783, L13
Pérez S., Casassus S., Baruteau C., Dong R., Hales A., Cieza L., 2019, AJ, 158, 15
Pinte C. et al., 2018, A&A, 609, A47
Rafikov R. R., 2002, ApJ, 569, 997
Regály Z., Juhász A., Sándor Z., Dullemond C. P., 2012, MNRAS, 419, 1701
Schöier F. L., van der Tak F. F. S., van Dishoeck E. F., Black J. H., 2005, A&A, 432, 369
Shakura N. I., Sunyaev R. A., 1973, A&A, 24, 337
Sierra A., Lizano S., Barge P., 2017, ApJ, 850, 115
Sierra A., Lizano S., Macías E., Carrasco-González C., Osorio M., Flock M., 2019, ApJ, 876, 7
Stahl O., Casassus S., Wilson T., 2008, A&A, 477, 865

Stolker T. et al., 2016, A&A, 595, A113
Stolker T. et al., 2017, ApJ, 849, 143
Teague R. et al., 2016, A&A, 592, A49
Teague R., Bae J., Bergin E. A., 2019, Nature, 574, 378
van der Marel N. et al., 2013, Science, 340, 1199
van der Marel N. et al., 2021, AJ, 161, 33
van der Marel N., van Dishoeck E. F., Bruderer S., Pérez L., Isella A., 2015a, A&A, 579, A106
van der Marel N., Pinilla P., Tobin J., van Kempen T., Andrews S., Ricci L., Birnstiel T., 2015b, ApJ, 810, L7
van der Marel N., van Dishoeck E. F., Bruderer S., Andrews S. M., Pontoppidan K. M., Herczeg G. J., van Kempen T., Miotello A., 2016a, A&A, 585, A58
van der Marel N., Cazzoletti P., Pinilla P., Garufi A., 2016b, ApJ, 832, 178
van der Plas G., Ménard F., Canovas H., Avenhaus H., Casassus S., Pinte C., Caceres C., Cieza L., 2017, A&A, 607, A55
van Holstein R. G. et al., 2020, A&A, 633, A64
Varnière P., Tagger M., 2006, A&A, 446, L13
Veronesi B., Lodato G., Dipierro G., Ragusa E., Hall C., Price D. J., 2019, MNRAS, 489, 3758
Wang L., Goodman J. J., 2017, ApJ, 835, 59
Weber P., Benítez-Llambay P., Gressel O., Krapp L., Pessah M. E., 2018, ApJ, 854, 153
Weidenschilling S. J., 1977, MNRAS, 180, 57
Wichittanakom C., Oudmaijer R. D., Fairlamb J. R., Mendigutía I., Vioque M., Ababakr K. M., 2020, MNRAS, 493, 234
Wilson T. L., Rood R., 1994, ARA&A, 32, 191
Xie C., Ren B., Dong R., Pueyo L., Ruffio J.-B., Fang T., Mawet D., Stolker T., 2021, ApJ, 906, L9
Yen H.-W., Gu P.-G., 2020, ApJ, 905, 89
Zhu Z., Baruteau C., 2016, MNRAS, 458, 3918
Zhu Z., Stone J. M., 2014, ApJ, 795, 53
Zhu Z., Dong R., Stone J. M., Rafikov R. R., 2015, ApJ, 813, 88

APPENDIX A: CHANNEL MAPS

Channels maps for the ^{12}CO(2-1) data are shown in Fig. A1 for the `tclean` imaging, and in Fig. A2 for the UVMEM image restoration. Both reconstructions used Briggs weighting to restore the visibility data, with a robustness parameter of 2. The UVMEM channels maps reach the same thermal noise as `tclean`, but with less extended negatives in the channels which correspond to emission which covers larger angular scales (near the systematic velocity). The channel maps for the *uv*-tapered versions of the UVMEM restorations, and for all isotopologues, are shown in Fig. A3.
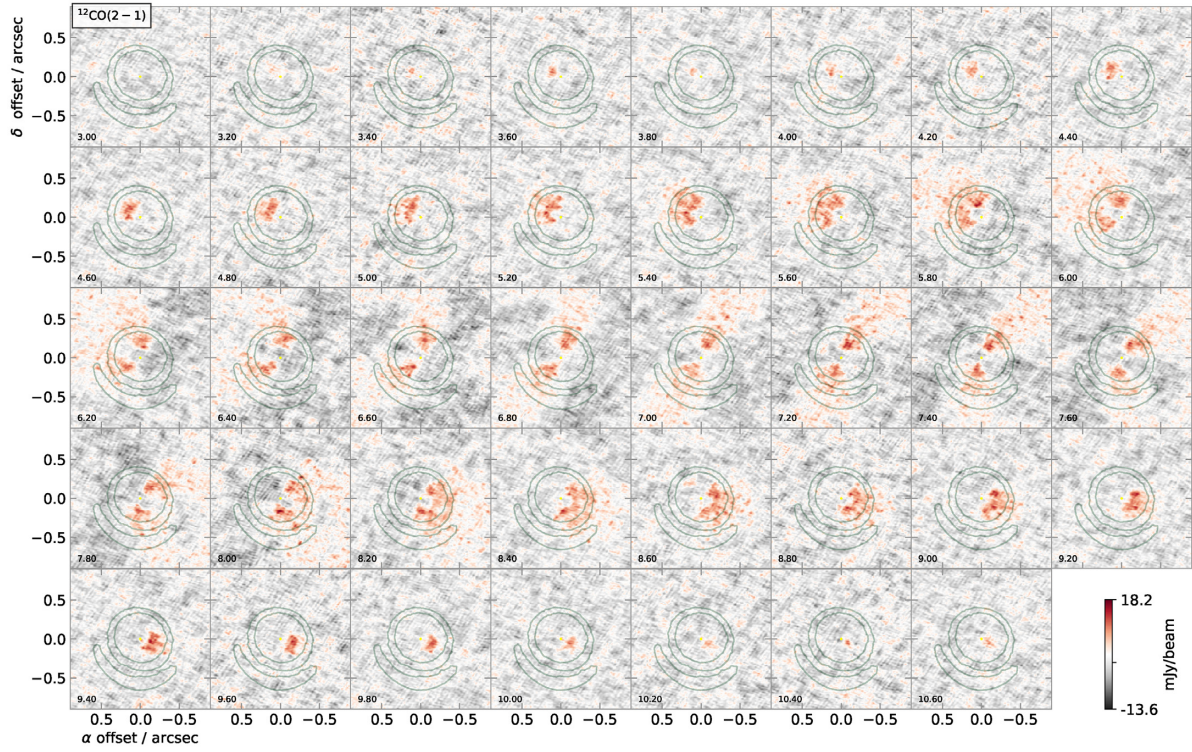
Figure A1. Channel maps from the `tclean` ^{12}CO(2−1) datacube. The continuum from Fig. 1 a is outlined in contours. The beam is $0\rlap{.}''054 \times 0\rlap{.}''040/89.4$ deg.
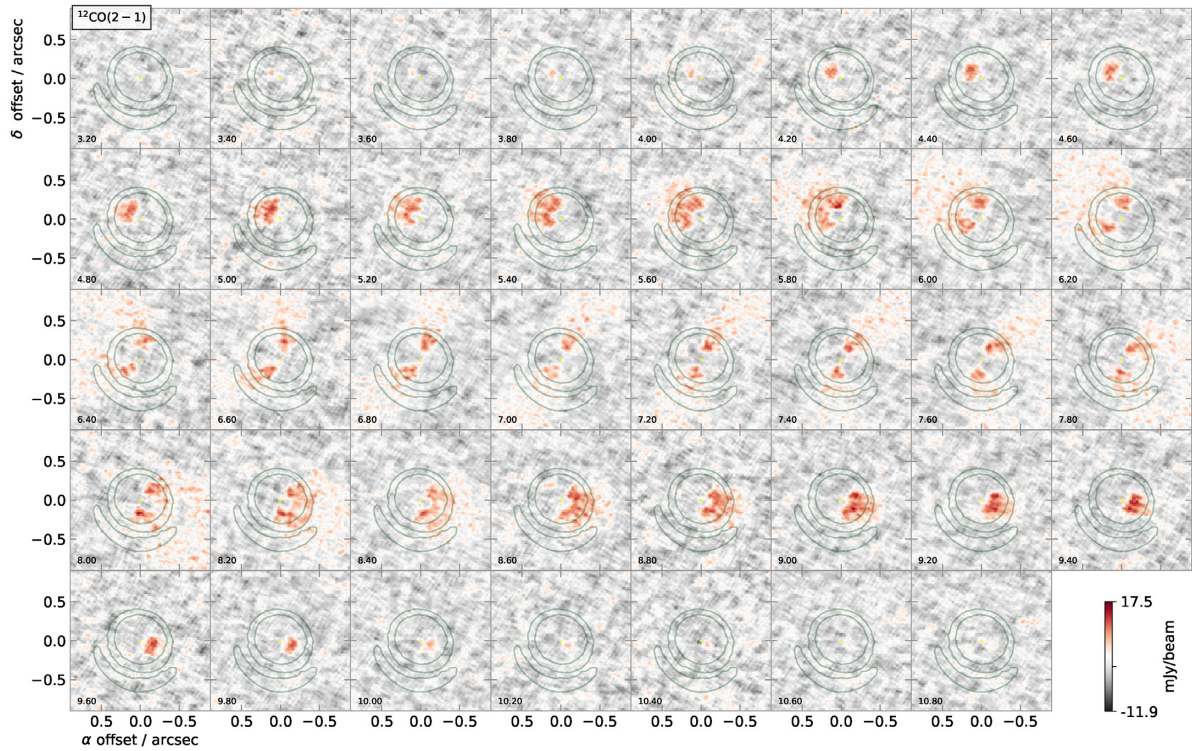

Figure A2. Channel maps from the UVMEM ^{12}CO(2-1) datacube. The continuum from Fig. 1a is outlined in contours. The beam is $0\rlap{.}''054 \times 0\rlap{.}''040/89.4$ deg.
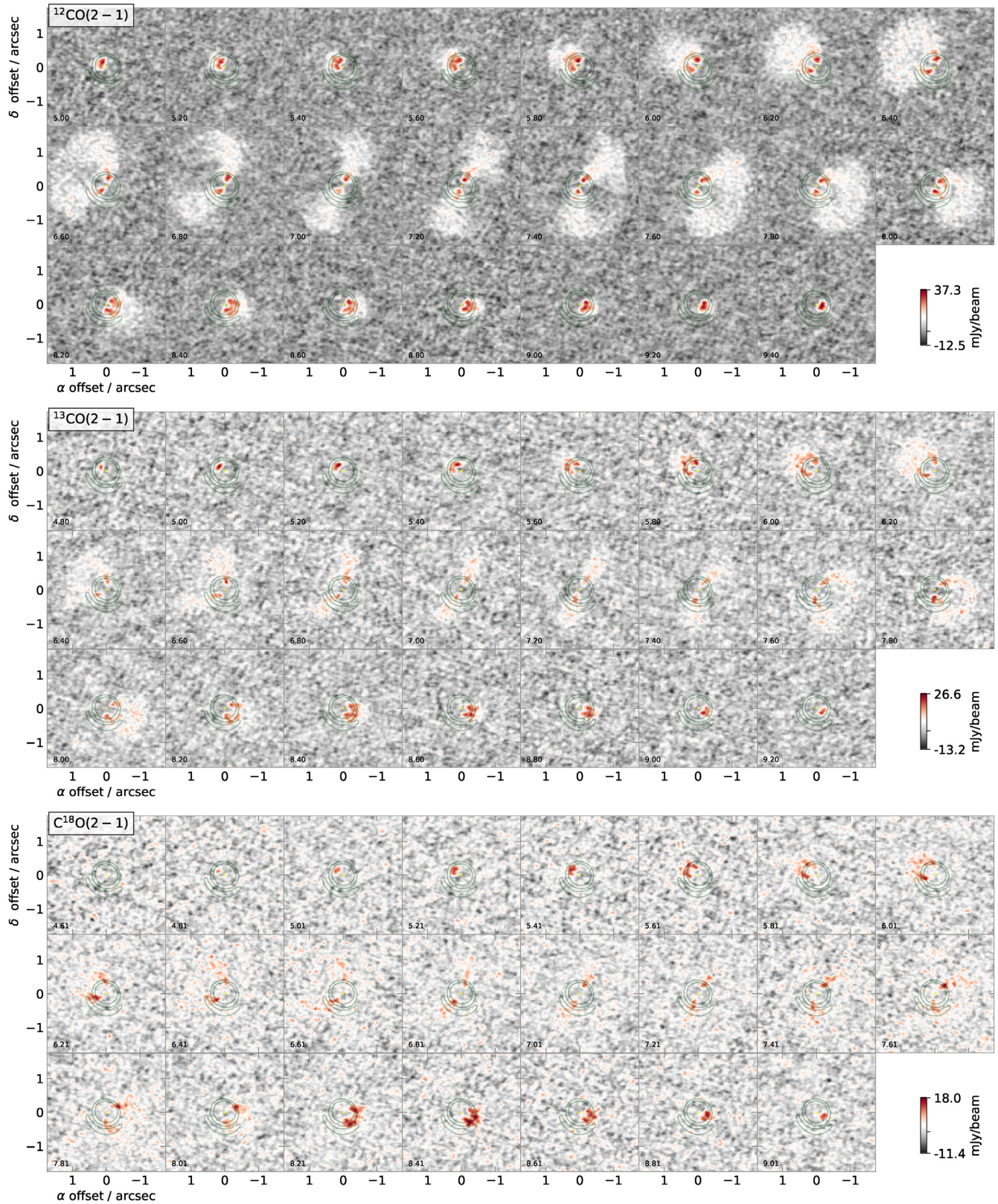
Figure A3. Channel maps from the UVMEM and *uv*−tapered datacubes for ^{12}CO(2-1), ^{13}CO(2-1) and C^{18}O(2-1). The continuum from Fig. 1a is outlined in contours. The beam is $0\rlap.{''}100 \times 0\rlap.{''}081/0$ deg.

APPENDIX B: DISC ORIENTATION FROM THE CONTINUUM

Disc orientation is often inferred from continuum data under the assumption of axial symmetry, either directly from visibility data (e.g. Jennings et al. 2020), or simply by fitting projected elliptical Gaussians in the image plane. Here we follow an image plane approach, under the assumption of axial symmetry for a thin disc (with null aspect ratio). We minimize the variance in the radial profile for the continuum intensity $I_\nu(R, \phi)$,

$$\chi^2_{\mathrm{var}} = \frac{1}{I^2_{\mathrm{noise}}} \sum_{l=l_1}^{l=l_2} \sigma^2_\phi(R_l; \mathrm{PA}, i, \Delta\alpha, \Delta\delta), \tag{B1}$$

where I_{noise} is the thermal noise in the image, and where σ^2_ϕ is the azimuthal variance of intensities,

$$\sigma^2_\phi(R_l) = \frac{1}{N_\phi} \sum_{k=0}^{N_\phi-1} (I_\nu(R_l, \phi_k) - \langle I_\nu(R_l) \rangle)^2, \tag{B2}$$

with

$$\langle I_\nu(R_l) \rangle = \frac{1}{N_\phi} \sum_{k=0}^{N_\phi-1} I_\nu(R_l, \phi_k). \tag{B3}$$

The radial profile $\langle I_\nu(R) \rangle$ and the variance $\sigma^2_\phi(R)$ profile depend on the disc position angle, inclination, and choice of origin for the (standard) polar expansion.

The minimization of $\chi^2_{\mathrm{var}}(\mathrm{PA}, i, \Delta\alpha, \Delta\delta)$ in equation (B1) is carried out with the EMCEE package (Foreman-Mackey et al. 2013), with flat priors, and with 600 iterations and 40 walkers. The resulting posterior distributions are summarized in Fig. B1 for an application to HD 135344B. This strategy to infer the disc orientation is implemented using Python in the MPOLARMAPS package, and is publicly available at git@github.com:simoncasassus/MPolarMaps.git.

APPENDIX C: STATISTICAL ANALYSIS OF THE LINE DIAGNOSTICS

As explained in Section 3.3, the uniform-slab parameters for the physical conditions along each line of sight are $(\log_{10}(\Sigma_g), \log_{10}(T_b), v_\circ, \log_{10}(v_{\mathrm{turb}}))$. The complete set of parameters resulting from an application of SLAB.LINE to HD 135344B, and their associated uncertainties, are shown in Figs C1 and C2, where we converted the logarithms to linear quantities. For conciseness the upwards and downwards uncertainties (corresponding to the 16 and 84 per cent quantiles) were averaged in a single 1σ error bar. Example fits are shown in Fig. C3.

Pure least-squares fit using equation (9) sometimes yielded glitches in the best-fitting parameters in particularly noisy lines of sights. After checking, in all regions with clear signal, that v_{turb} was subsonic and that the optical depth in thinnest transition ($^{18}CO(2\text{-}1)$) was everywhere less than 5, we controlled these glitches by adding
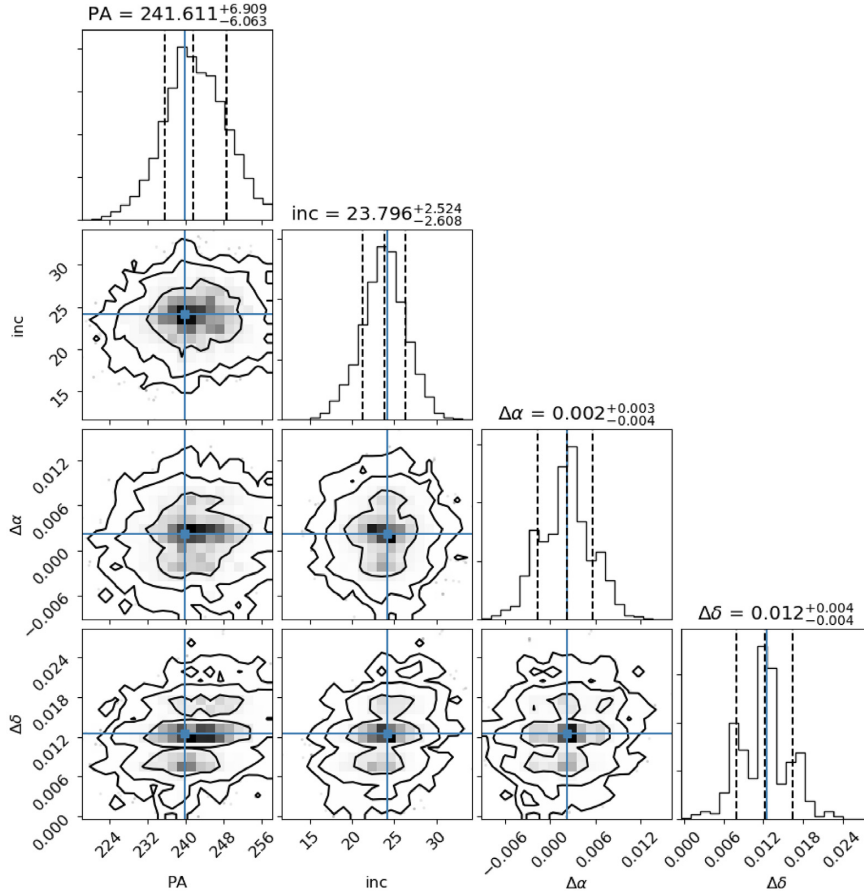

Figure B1. Corner plot from the χ^2_{var} optimization of the orientation parameters in HD 135344B using the `tclean` continuum image at 225 GHz continuum from Fig. 1b.
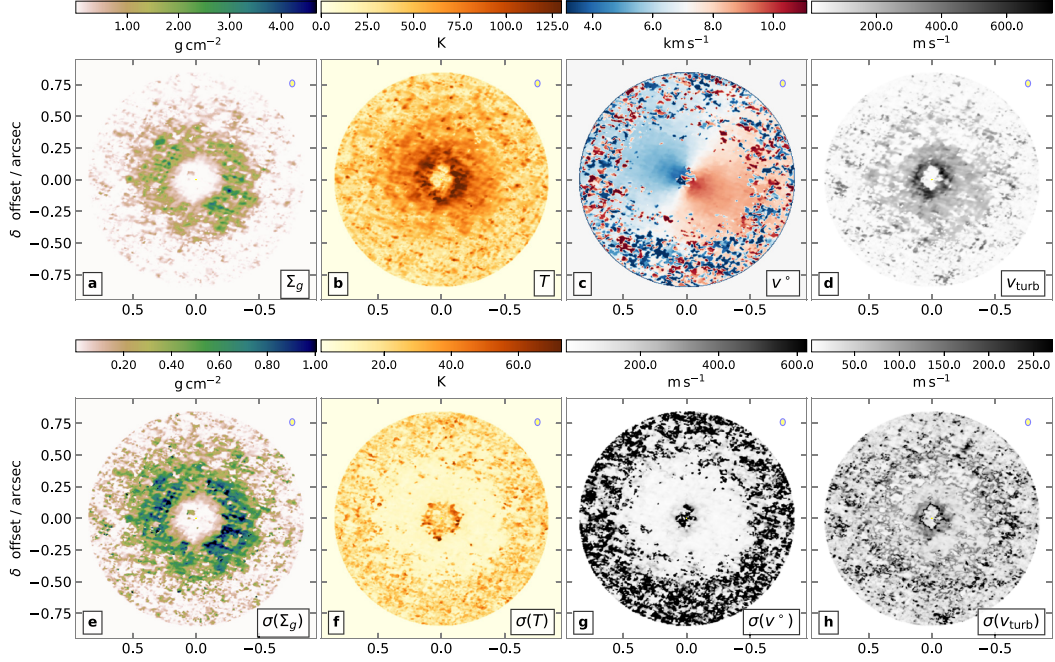
Figure C1. Expectation values and associated 1σ errors for an application of SLAB.LINE to the original CO(2-1) isotopologues data (no taper).
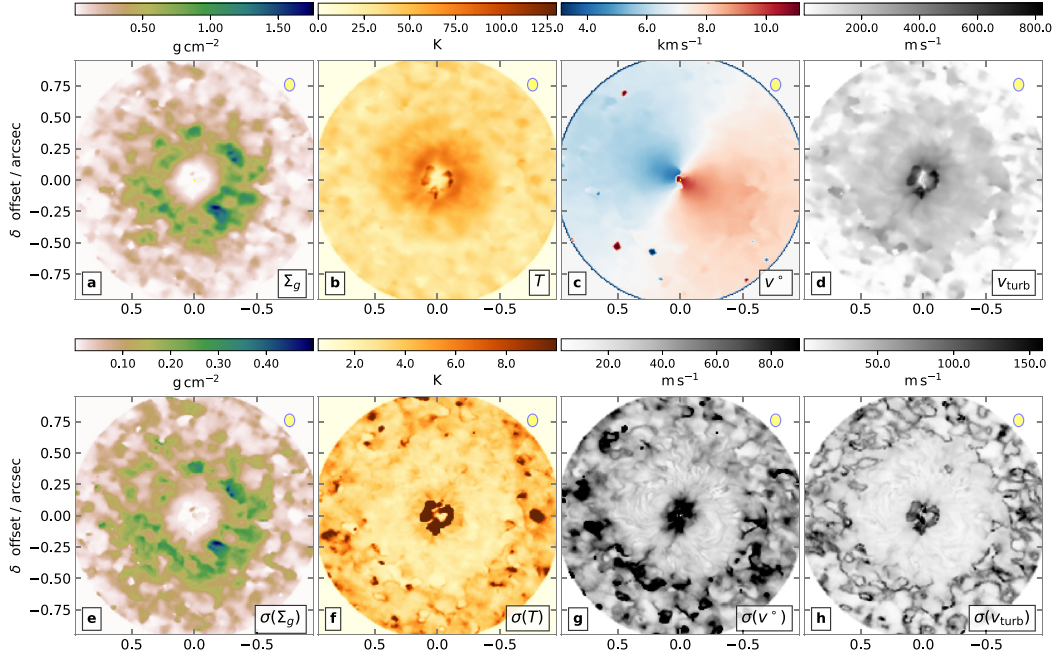

Figure C2. Same as Fig. C1 but for the *uv*-tapered data.

two regularization terms. The final log-likelihood is

$$
L = -\frac{1}{2}\chi^2 + \lambda_{v_{\text{turb}}} H\left[\frac{(v_{\text{turb}} - c_s)}{c_s}\right]\left(\frac{(v_{\text{turb}} - c_s)}{c_s}\right)^2
$$
$$
+ \lambda_\tau H\left[\min\left(\{\tau_{\circ,i}\}_{i=1}^{N_{\text{iso}}}\right) - \Gamma_\circ\right]\left(\min\left(\{\tau_{\circ,i}\}_{i=1}^{N_{\text{iso}}}\right) - \Gamma_\circ\right)^2,
$$

(C1)

where χ^2 is given by equation (9), H represents the Heaviside step function and $\min(\tau_\circ, i_{i=1}^{N_{\text{iso}}})$ represents the minimum optical depth at

the line centre for the N_{iso} isotopologues involved in the fit. We used $\lambda_{v_{\text{turb}}} = 100$, $\lambda_\tau = 1$ and a threshold optical depth $\Gamma_\circ = 5$.

An example corner plot, for the line of sight labelled '1' in Fig. C3 (right, without a *uv*-taper), is shown in Fig. C4. This example line of sight has copious signal in ^{13}CO(2-1) and leads to well-constrained expectation values. However, the line of sight labelled '0' in Fig. C3 (right, without a *uv*-taper) falls inside the dust ring ring and only ^{12}CO(2-1) is picked up. The posterior distribution of the SLAB.LINE parameters are strongly correlated, as shown in Fig. C5.
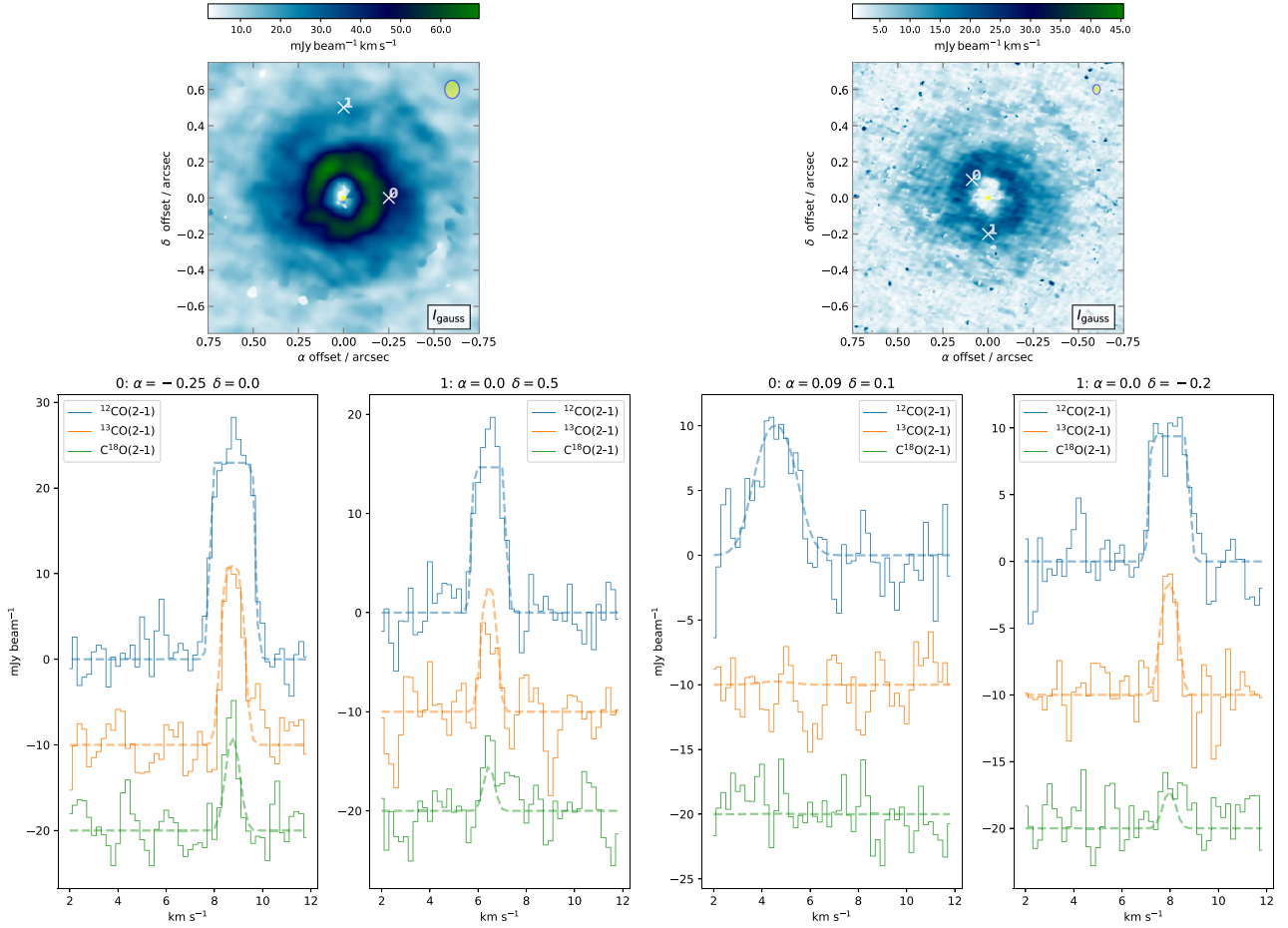
Figure C3. Comparison of observed and best-fitting SLAB.LINE spectra for selected lines of sights, at the offset R.A. (α) and Dec. (δ) reported as titles to the spectral profiles, and also shown in the image at the top. The observed spectra are drawn in solid lines, while the model is shown in thick dashed lines. Left: SLAB.LINE fits on the *uv*-tapered datacubes. Right: SLAB.LINE fits on the original datacubes (no taper).

The regularization terms used in equation (C1) have no impact in this case, and we controlled such noisy lines of sight by imposing an upper limit temperature of $3\times$ the $^{12}CO(2\text{-}1)$ peak brightness temperature. If instead we set an absolute maximum temperature, for instance 500 K, then the maps shown in Figs C1 and C2 are unchanged except for T, which reaches somewhat higher values inside the cavity but is modulated by noisy spikes in the outer regions where only $^{12}CO(2\text{-}1)$ is picked up.
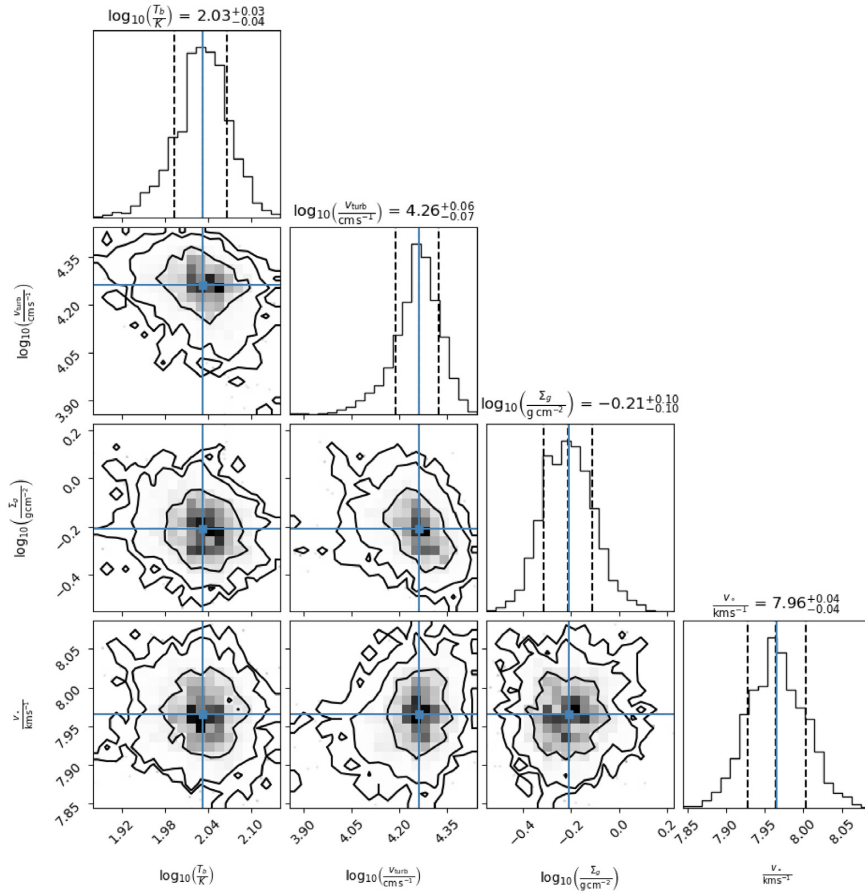
Figure C4. Corner plot for the posterior distribution of the SLAB.LINE parameters in the line of sight labelled '1' in Fig. C3 (right).
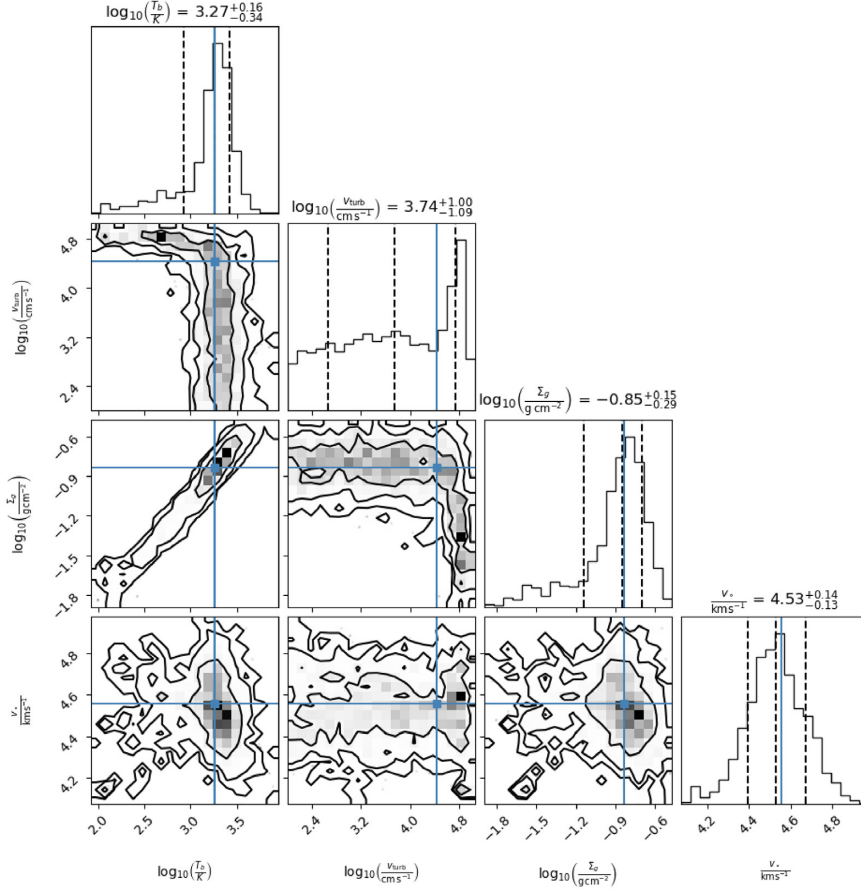
Figure C5. Same as Fig. C4 for the line of sight labelled '0' in Fig. C3 (right).

[1] *Departamento de Astronomía, Universidad de Chile, Casilla 36-D, Santiago, Chile*

[2] *School of Physics and Astronomy, Monash University, Clayton Vic 3800, Australia*

[3] *Jodrell Bank Centre for Astrophysics, Department of Physics and Astronomy, University of Manchester, Alan Turing Building, Oxford Road, Manchester, M13 9PL, UK*

[4] *University of Santiago of Chile (USACH), Faculty of Engineering, Computer Engineering Department, Chile*

[5] *Center for Interdisciplinary Research in Astrophysics and Space Exploration (CIRAS), Universidad de Santiago deChile*

[6] *Departamento de Física, Universidad de Santiago de Chile, Avenida Ecuador 3493, Estación Central, Santiago, Chile*

[7] *Universitäts-Sternwarte, Ludwig-Maximilians-Universität München, Scheinerstr. 1, 81679 München, Germany*

[8] *Department of Physics & Astronomy, University of Victoria, Victoria, BC, V8P 1A1, Canada*

[9] *University of Grenoble Alpes, CNRS, IPAG, F-38000 Grenoble, France*

[10] *IRAP, Université de Toulouse, CNRS, UPS, Toulouse, France*

[11] *Núcleo de Astronomía, Facultad de Ingeniería y Ciencias, Universidad Diego Portales, Av Ejército 441, Santiago, Chile*

[12] *Leiden Observatory, Leiden University, PO Box 9513, 2300 RA Leiden, The Netherlands*

[13] *Max-Plank-Institut fur Extraterrestrische Physik, Giessenbachstrasse 1, D-85748 Garching, Germany*

[14] *Facultad de Ingeniería y Ciencias, Universidad Adolfo Ibáñez, Av. Diagonal las Torres 2640, Peñalolén, Santiago, Chile*

[15] *Millennium Institute for Astrophysics, Chile*

[16] *STAR Institute, Université de Liège, 19c Allée du Six Août, 4000 Liège, Belgium*

[17] *Jet Propulsion Laboratory, California Institute of Technology, 4800 Oak Grove drive, Pasadena CA 91109, USA*

[18] *Institute for Astronomy, University of Hawaii at Manoa, 640 N. Aohoku Place, Hilo, HI 96720, USA*

[19] *Institute of Astronomy, KU Leuven, Celestijnenlaan 200D, B-3001 Leuven, Belgium*

This paper has been typeset from a TeX/LaTeX file prepared by the author.